A&A 486, 359–373 (2008)
DOI: 10.1051/0004-6361:200809538

Astronomy & Astrophysics

# Radial temperature profiles for a large sample of galaxy clusters observed with *XMM-Newton*[⋆]

A. Leccardi[1,2] and S. Molendi[2]

[1] Università degli Studi di Milano, Dip. di Fisica, via Celoria 16, 20133 Milano, Italy
[2] INAF-IASF Milano, via Bassini 15, 20133 Milano, Italy
e-mail: `leccardi@iasf-milano.inaf.it`

Received 8 February 2008 / Accepted 8 April 2008

## ABSTRACT

*Aims.* We measure radial temperature profiles as far out as possible for a sample of ≈50 hot, intermediate redshift galaxy clusters, selected from the *XMM-Newton* archive, keeping systematic errors under control.

*Methods.* Our work is characterized by two major improvements. First, we used background modeling, rather than background subtraction, and the Cash statistic rather than the $\chi^2$. This method requires a careful characterization of all background components. Second, we assessed systematic effects in detail. We performed two groups of tests. Prior to the analysis, we made use of extensive simulations to quantify the impact of different spectral components on simulated spectra. After the analysis, we investigated how the measured temperature profile changes, when choosing different key parameters.

*Results.* The mean temperature profile declines beyond 0.2 $R_{180}$. For the first time, we provide an assessment of the source and the magnitude of systematic uncertainties. When comparing our profile with those obtained from hydrodynamic simulations, we find the slopes beyond ≈0.2 $R_{180}$ to be similar. Our mean profile is similar but somewhat flatter with respect to those obtained by previous observational works, possibly as a consequence of a different level of characterizing systematic effects.

*Conclusions.* This work allows us to not only constrain cluster temperature profiles in outer regions with confidence, but also, from a more general point of view, to explore the limits of the current X-ray experiments (in particular *XMM-Newton*) with respect to the analysis of low surface-brightness emission.

**Key words.** X-rays: galaxies: clusters – galaxies: clusters: general – cosmology: observations

## 1. Introduction

Clusters of galaxies are the most massive gravitationally bound systems in the universe. They are permeated by the hot, X-ray emitting, intra-cluster medium (ICM), which represents the dominant baryonic component. The key ICM observable quantities are its density, temperature, and metallicity. Assuming hydrostatic equilibrium, the gas temperature and density profiles allow us to derive the total cluster mass and thus to use galaxy clusters as cosmological probes (e.g. Henry & Arnaud 1991; Ettori et al. 2002; Fabian & Allen 2003; Voit 2005). Temperature and density profiles can also be combined to determine the ICM entropy distribution, which provides valuable information on the cluster thermodynamic history and has proven to be a powerful tool in investigating non-gravitational processes (e.g. Ponman et al. 2003; McCarthy et al. 2004; Voit 2005; Pratt et al. 2006).

The outer regions of clusters are rich in information and interesting to study, because clusters are still forming there by accretion (e.g. Tozzi et al. 2000; Borgani et al. 2004). Moreover, far from the core it is easier to compare simulations with observations, because feedback effects are less important (e.g. Borgani et al. 2004; McNamara et al. 2005; Roncarelli et al. 2006). Cluster surface brightness rapidly declines with radius, while background (of instrumental, solar, local, and cosmic origin) is roughly constant over the detector. For this reason, spectra accumulated in the outer regions are characterized by poor statistics and high background, especially at high energies, where the instrumental background dominates other components. These conditions make temperature measurement at large distances from the center a technically challenging task, requiring an adequate treatment of both statistical and systematic issues (Leccardi & Molendi 2007).

Given the technical difficulties, early measurements of cluster temperature profiles have been controversial. At the end of the *ASCA* and *BeppoSAX* era, the shape of the profiles at large radii was still the subject of debate (Markevitch et al. 1998; Irwin et al. 1999; White 2000; Irwin & Bregman 2000; Finoguenov et al. 2001; De Grandi & Molendi 2002). Recent observations with current experiments (i.e. *XMM-Newton* and *Chandra*) have clearly shown that cluster temperature profiles decline beyond the 15−20% of $R_{180}$ (Piffaretti et al. 2005; Vikhlinin et al. 2005; Pratt et al. 2007; Snowden et al. 2008). However, most of these measurements might be unreliable at very large radii (≳50% of $R_{180}$) because they are affected by a number of systematics related to the analysis technique and to the background treatment (Leccardi & Molendi 2007).

The aim of this work is to measure the mean temperature profile of galaxy clusters as far out as possible, while keeping systematic errors under control. From the *XMM-Newton*

---

[⋆] Appendices A and B are only available in electronic form at `http://www.aanda.org`

Article published by EDP Sciences

archive, we selected all hot ($kT > 3.5$ keV), intermediate redshift ($0.1 \lesssim z \lesssim 0.3$) clusters that are not strongly interacting and measured their radial temperature profiles. The spectral analysis followed a new approach by using the background modeling rather than the background subtraction, and the Cash statistic rather than the $\chi^2$. This method requires a careful characterization (reported in the Appendices) of all background components, which unfortunately was not possible for EPIC-pn. For this reason, we used only EPIC-MOS data in our analysis.

Background parameters are estimated in a peripheral region, where the cluster emission is almost negligible, and rescaled in the regions of interest. The spectral fitting is performed in the 0.7–10.0 keV and in the 2.0–10.0 keV energy bands, which are characterized by different statistics and level of systematics, to check the consistency of our results. A second important point is a particular attention to systematic effects. We performed two groups of test: prior to the analysis, we made use of extensive simulations to quantify the impact of different components (e.g. the cosmic variance or the soft proton contribution) on simulated spectra; after the analysis, we investigated how the measured temperature profile changes, when choosing different key parameters (e.g. the truncation radius or the energy band). At the end of our tests, we provided an assessment of the source and the magnitude of systematic uncertainties associated to the mean profile.

The outline of the paper is the following. In Sect. 2 we describe sample properties and selection criteria and in Sect. 3 we describe our data analysis technique in detail. In Sect. 4 we present the radial temperature profiles for all clusters in our sample and compute the average profile. In Sect. 5 we describe our analysis of systematic effects. In Sect. 6 we characterize the profile decline, investigate its dependency from physical properties (e.g. the redshift), and compare it with hydrodynamic simulations and previous observational works. Our main results are summarized in Sect. 7. In the Appendices we report the analysis of closed and blank field observations, which allows us to characterize most background components.

Quoted confidence intervals are 68% for one interesting parameter (i.e. $\Delta C = 1$), unless otherwise stated. All results are given assuming a $\Lambda$CDM cosmology with $\Omega_{\rm m} = 0.3$, $\Omega_\Lambda = 0.7$, and $H_0 = 70$ km s$^{-1}$ Mpc$^{-1}$.

## 2. The sample

We selected from the *XMM-Newton* archive a sample of hot ($kT > 3.3$ keV), intermediate redshift ($0.1 \lesssim z \lesssim 0.3$), and high galactic latitude ($|b| > 20°$) clusters of galaxies. Upper and lower limits to the redshift range are determined, respectively, by the cosmological dimming effect and the size of the EPIC field of view ($\approx 15'$ radius). Indeed, our data analysis technique requires that the intensity of background components be estimated in a peripheral region, where the cluster emission is almost negligible (see Sect. 3.2.1). We retrieved from the public archive all observations of clusters satisfying the above selection criteria, performed before March 2005 (when the CCD6 of EPIC-MOS1 was switched off[1]) and available at the end of May 2007. Unfortunately, 23 of these 86 observations are highly affected by soft proton flares (see Table 1). We excluded them from the sample, because their good (i.e. after flare cleaning, see Sect. 3.1.1) exposure time is not long enough (less than 16 ks when summing MOS1 and MOS2) to measure reliable temperature profiles out to external regions. Furthermore, we excluded 14 observations of clusters that show evidence of recent and strong interactions (see Table 2). For such clusters, a radial analysis is not appropriate, because the gas distribution is far from being azimuthally symmetric. Finally, we find that the target of observation 0201901901, which is classified as a cluster, is probably a point-like source; therefore, we excluded this observation too from our sample.

In Table 3 we list the 48 observations that survived our selection criteria and report cluster physical properties. The redshift value (from optical measurements) is taken from the NASA Extragalactic Database[2]; $kT_{\rm M}$ and $R_{180}$ are derived from our analysis (see Sect. 4). In Fig. 1 we report the cluster distribution in the redshift-temperature space. The only selection effect we detect is the paucity of cool ($kT_{\rm M} \lesssim 5$ keV) clusters at high ($z > 0.2$) redshift. Observations were performed with THIN1 and MEDIUM filters, as reported in Table 3.

**Table 1.** Observations excluded from the sample due to high soft proton contamination.

| Name | Obs ID |
|---|---|
| RXC J0303.8-7752 | 0042340401 |
| RXC J0516.7-5430 | 0042340701 |
| RXC J0528.9-3927 | 0042340801 |
| RXC J2011.3-5725 | 0042341101 |
| Abell 2537 | 0042341201 |
| RXC J0437.1+0043 | 0042341601 |
| Abell 1302 | 0083150401 |
| Abell 2261 | 0093030301 |
| Abell 2261 | 0093030801 |
| Abell 2261 | 0093030901 |
| Abell 2261 | 0093031001 |
| Abell 2261 | 0093031101 |
| Abell 2261 | 0093031401 |
| Abell 2261 | 0093031501 |
| Abell 2261 | 0093031601 |
| Abell 2261 | 0093031801 |
| Abell 2219 | 0112231801 |
| Abell 2219 | 0112231901 |
| RXC J0006.0-3443 | 0201900201 |
| RXC J0145.0-5300 | 0201900501 |
| RXC J0616.8-4748 | 0201901101 |
| RXC J0437.1+0043 | 0205330201 |
| Abell 2537 | 0205330501 |

**Table 2.** Observations of clusters that show evidence of recent and strong interactions.

| Name | Obs ID |
|---|---|
| Abell 2744 | 0042340101 |
| Abell 665 | 0109890401 |
| Abell 665 | 0109890501 |
| Abell 1914 | 0112230201 |
| Abell 2163 | 0112230601 |
| Abell 2163 | 0112231501 |
| RXC J0658.5-5556 | 0112980201 |
| Abell 1758 | 0142860201 |
| Abell 1882 | 0145480101 |
| Abell 901 | 0148170101 |
| Abell 520 | 0201510101 |
| Abell 2384 | 0201902701 |
| Abell 115 | 0203220101 |
| ZwCl2341.1+0000 | 0211280101 |

---

[1] http://xmm.esac.esa.int/external/xmm_news/items/MOS1-CCD6/index.shtml

[2] http://nedwww.ipac.caltech.edu

**Table 3.** Physical properties and observation details for the 48 clusters of our sample.

| Name | Obs ID | $z^a$ | $kT_M{}^b$ | $R_{180}{}^c$ | Exp. time$^d$ | | $R_{SB}{}^e$ | Filter |
|---|---|---|---|---|---|---|---|---|
| RXC J0043.4-2037 | 0042340201 | 0.2924 | 6.8 | 1.78 | 11.9 | 11.3 | 1.25 | THIN1 |
| RXC J0232.2-4420 | 0042340301 | 0.2836 | 7.2 | 1.85 | 12.1 | 11.7 | 1.08 | THIN1 |
| RXC J0307.0-2840 | 0042340501 | 0.2534 | 6.8 | 1.82 | 11.4 | 12.6 | 1.08 | THIN1 |
| RXC J1131.9-1955 | 0042341001 | 0.3072 | 8.1 | 1.93 | 12.4 | 12.3 | 1.08 | THIN1 |
| RXC J2337.6+0016 | 0042341301 | 0.2730 | 7.2 | 1.86 | 13.4 | 13.1 | 1.19 | THIN1 |
| RXC J0532.9-3701 | 0042341801 | 0.2747 | 7.5 | 1.90 | 10.9 | 10.5 | 1.09 | THIN1 |
| Abell 68 | 0084230201 | 0.2550 | 7.2 | 1.88 | 26.3 | 25.9 | 1.37 | MEDIUM |
| Abell 209 | 0084230301 | 0.2060 | 6.6 | 1.85 | 17.9 | 17.8 | 1.19 | MEDIUM |
| Abell 267 | 0084230401$^*$ | 0.2310 | 4.5 | 1.49 | 17.0 | 16.5 | 1.79 | MEDIUM |
| Abell 383 | 0084230501 | 0.1871 | 4.4 | 1.52 | 29.3 | 29.8 | 1.33 | MEDIUM |
| Abell 773 | 0084230601 | 0.2170 | 7.5 | 1.96 | 13.6 | 15.5 | 1.16 | MEDIUM |
| Abell 963 | 0084230701 | 0.2060 | 6.5 | 1.83 | 24.4 | 26.0 | 1.19 | MEDIUM |
| Abell 1763 | 0084230901 | 0.2230 | 7.2 | 1.92 | 13.0 | 13.2 | 1.08 | MEDIUM |
| Abell 1689 | 0093030101 | 0.1832 | 9.2 | 2.21 | 36.8 | 36.8 | 1.14 | THIN1 |
| RX J2129.6+0005 | 0093030201 | 0.2350 | 5.5 | 1.66 | 36.0 | 37.5 | 1.21 | MEDIUM |
| ZW 3146 | 0108670101 | 0.2910 | 7.0 | 1.81 | 52.9 | 52.9 | 1.07 | THIN1 |
| E1455+2232 | 0108670201 | 0.2578 | 5.0 | 1.56 | 35.3 | 35.8 | 1.11 | MEDIUM |
| Abell 2390 | 0111270101 | 0.2280 | 11.2 | 2.37 | 9.9 | 10.3 | 1.11 | THIN1 |
| Abell 2204 | 0112230301 | 0.1522 | 8.5 | 2.16 | 18.2 | 19.5 | 1.06 | MEDIUM |
| Abell 1413 | 0112230501 | 0.1427 | 6.7 | 1.92 | 25.4 | 25.4 | 1.10 | THIN1 |
| Abell 2218 | 0112980101 | 0.1756 | 6.5 | 1.86 | 18.2 | 18.2 | 1.17 | THIN1 |
| Abell 2218 | 0112980401 | 0.1756 | 7.0 | 1.93 | 13.7 | 14.0 | 1.42 | THIN1 |
| Abell 2218 | 0112980501 | 0.1756 | 6.1 | 1.80 | 11.3 | 11.0 | 1.07 | THIN1 |
| Abell 1835 | 0147330201 | 0.2532 | 8.6 | 2.05 | 30.1 | 29.2 | 1.16 | THIN1 |
| Abell 1068 | 0147630101 | 0.1375 | 4.5 | 1.58 | 20.5 | 20.8 | 1.09 | MEDIUM |
| Abell 2667 | 0148990101 | 0.2300 | 7.7 | 1.96 | 21.9 | 21.6 | 1.48 | MEDIUM |
| Abell 3827 | 0149670101 | 0.0984 | 7.1 | 2.02 | 22.3 | 22.4 | 1.16 | MEDIUM |
| Abell 3911 | 0149670301 | 0.0965 | 5.4 | 1.77 | 25.8 | 26.1 | 1.43 | THIN1 |
| Abell 2034 | 0149880101 | 0.1130 | 7.0 | 1.99 | 10.2 | 10.5 | 1.16 | THIN1 |
| RXC J0003.8+0203 | 0201900101 | 0.0924 | 3.7 | 1.47 | 26.3 | 26.6 | 1.10 | THIN1 |
| RXC J0020.7-2542 | 0201900301 | 0.1424 | 5.7 | 1.78 | 14.8 | 15.4 | 1.02 | THIN1 |
| RXC J0049.4-2931 | 0201900401 | 0.1080 | 3.3 | 1.37 | 19.2 | 18.8 | 1.28 | THIN1 |
| RXC J0547.6-3152 | 0201900901 | 0.1483 | 6.7 | 1.92 | 23.3 | 24.0 | 1.12 | THIN1 |
| RXC J0605.8-3518 | 0201901001 | 0.1410 | 4.9 | 1.65 | 18.0 | 24.1 | 1.07 | THIN1 |
| RXC J0645.4-5413 | 0201901201 | 0.1670 | 7.1 | 1.95 | 10.9 | 10.9 | 1.11 | THIN1 |
| RXC J1044.5-0704 | 0201901501 | 0.1323 | 3.9 | 1.47 | 25.7 | 25.9 | 1.03 | THIN1 |
| RXC J1141.4-1216 | 0201901601 | 0.1195 | 3.8 | 1.46 | 28.4 | 28.6 | 1.03 | THIN1 |
| RXC J1516.3+0005 | 0201902001 | 0.1183 | 5.3 | 1.73 | 26.7 | 26.6 | 1.13 | THIN1 |
| RXC J1516.5-0056 | 0201902101 | 0.1150 | 3.8 | 1.46 | 30.0 | 30.0 | 1.08 | THIN1 |
| RXC J2014.8-2430 | 0201902201 | 0.1612 | 7.1 | 1.96 | 23.0 | 23.4 | 1.05 | THIN1 |
| RXC J2048.1-1750 | 0201902401 | 0.1470 | 5.6 | 1.75 | 24.6 | 25.3 | 1.07 | THIN1 |
| RXC J2149.1-3041 | 0201902601 | 0.1179 | 3.3 | 1.37 | 25.1 | 25.5 | 1.11 | THIN1 |
| RXC J2218.6-3853 | 0201903001 | 0.1379 | 6.4 | 1.88 | 20.2 | 21.4 | 1.11 | THIN1 |
| RXC J2234.5-3744 | 0201903101 | 0.1529 | 8.6 | 2.17 | 18.9 | 19.3 | 1.31 | THIN1 |
| RXC J0645.4-5413 | 0201903401 | 0.1670 | 8.5 | 2.13 | 11.5 | 12.1 | 1.51 | THIN1 |
| RXC J0958.3-1103 | 0201903501 | 0.1527 | 6.1 | 1.83 | 8.3 | 9.4 | 1.16 | THIN1 |
| RXC J0303.8-7752 | 0205330101 | 0.2742 | 7.5 | 1.89 | 11.7 | 11.5 | 1.18 | THIN1 |
| RXC J0516.7-5430 | 0205330301 | 0.2952 | 7.5 | 1.87 | 11.4 | 11.7 | 1.19 | THIN1 |

Notes. $^a$ Redshift taken from the NASA Extragalactic Database; $^b$ mean temperature in keV derived from our analysis; $^c$ scale radius in Mpc derived from our analysis; $^d$ MOS1 and MOS2 good exposure time in ks; $^e$ intensity of residual soft protons (see Eq. (1)); $^*$ excluded due to high residual soft proton contamination.

## 3. Data analysis

The preparation of spectra comprises the following major steps:

- preliminary data processing;
- good time interval (GTI) filtering to exclude periods of high soft proton flux;
- filtering according to pattern and flag criteria;
- excision of brightest point-like sources;
- calculation of the “IN over OUT” ratio;
- extraction of spectra in concentric rings.

The spectral analysis is structured as follows:

- estimate of background parameters from a peripheral ring of the field of view;
- spectral fitting using the Cash statistic and modeling the background, rather than subtracting it, as commonly done;
- production of surface brightness, temperature, and metallicity profiles.

All these points are described in detail in the following subsections.

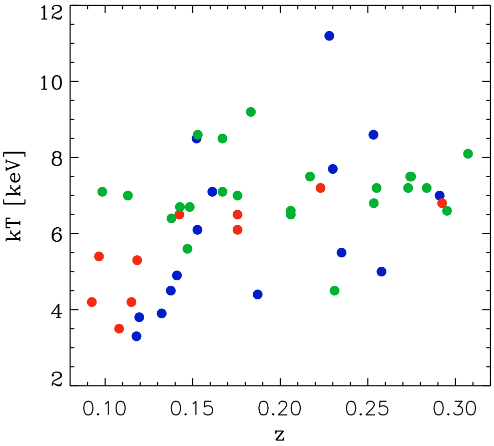

**Fig. 1.** Distribution of selected clusters in the redshift-temperature space. We distinguish cool core (blue), non cool core (red) and uncertain (green) clusters, as defined in Sect. 6. There is no evidence of selection effects, except for a weak positive correlation between redshift and temperature.

In our analysis we used only EPIC-MOS data, because a robust characterization of EPIC-pn background was not possible, mainly due to the small regions outside the field of view and to the non-negligible fraction of out of time events (for further details, see Appendix B). Moreover, the EPIC-pn background is less stable than the EPIC-MOS one, especially below 2 keV.

### 3.1. *Spectra preparation*

#### 3.1.1. Preliminary data preparation

Observation data files (ODF) were retrieved from the *XMM-Newton* archive and processed in a standard way with the Science Analysis System (SAS) v6.1.

The soft proton cleaning was performed using a double filtering process. We extracted a light curve in 100 s bins in the 10–12 keV energy band by excluding the central CCD, applied a threshold of 0.20 cts $s^{-1}$, produced a GTI file and generated the filtered event file accordingly. This first step allows most flares to be eliminated, however softer flares may exist such that their contribution above 10 keV is negligible. We then extracted a light curve in the 2–5 keV band and fit the histogram obtained from this curve with a Gaussian distribution. Since most flares had been rejected in the previous step, the fit was usually very good. We calculated the mean count rate, $\mu$, and the standard deviation, $\sigma$, applied a threshold of $\mu + 3\sigma$ to the distribution, and generated the filtered event file.

After soft proton cleaning, we filtered the event file according to `PATTERN` and `FLAG` criteria (namely `PATTERN` $\leq$ 12 and `FLAG` == 0). In Table 3 we report the good exposure time after the soft proton cleaning; as mentioned in Sect. 2, we excluded observations for which the total (MOS1+MOS2) good exposure time is less than 16 ks. In the left panel of Fig. 2 we report the histogram of the frequency distribution for observation exposure times.

When fitting spectra in the 0.7–10.0 keV band (see Sect. 3.2), we also excluded the "bright" CCDs, i.e. CCD-4 and CCD-5 for MOS1 and CCD-2 and CCD-5 for MOS2 (see Appendix A for the discussion).

Brightest point-like sources were detected, using a procedure based on the SAS task `edetect_chain` and excluded from the event file. We estimated a flux limit for excluded sources on the order of $10^{-13}$ erg $cm^{-2}$ $s^{-1}$; after the source excision, the cosmic variance of the X-ray background on the entire field of view is ≈20%.

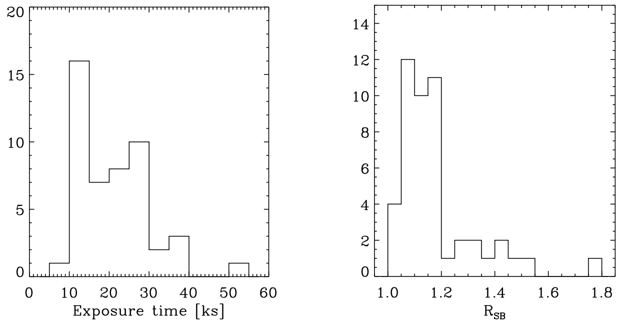

**Fig. 2.** Histograms of the frequency distribution for averaged MOS exposure time (*left panel*) and $R_{SB}$ (*right panel*) values.

#### 3.1.2. Quiescent soft proton contamination

A quiescent soft proton (QSP) component can survive the double filtering process (see Sect. 3.1.1). To quantify the amount of this component, we made use of the "IN over OUT" diagnostic[3] (De Luca & Molendi 2004). We measured the surface brightness, $SB_{IN}$, in an outer region of the field of view, where the cluster emission is negligible, and compared it to the surface brightness, $SB_{OUT}$, calculated outside the field of view in the same energy range (i.e. 6–12 keV). Since soft protons are channeled by the telescope mirrors inside the field of view and the cosmic ray induced background covers the whole detector, the ratio

$$R_{SB} = \frac{SB_{IN}}{SB_{OUT}} \tag{1}$$

is a good indicator of the intensity of residual soft protons and is used for background modeling (see Sect. 3.2.2 and Appendix B). In Table 3 we report the values of $R_{SB}$ for each observation. They roughly span the range from 1.0 (negligible contamination) to 1.5 (high contamination). The typical uncertainty in measuring $R_{SB}$ is a few percent. In the right panel of Fig. 2 we report the frequency distribution for $R_{SB}$ values. Since the observation 0084230401 of Abell 267 is extremely polluted by QSP ($R_{SB}$ = 1.8), we excluded it from the sample.

#### 3.1.3. Spectra accumulation

The cluster emission was divided in 10 concentric rings (namely 0′–0.5′, 0.5′–1′, 1′–1.5′, 1.5′–2′, 2′–2.75′, 2.75′–3.5′, 3.5′–4.5′, 4.5′–6′, 6′–8′, and 10′–12′). The center of the rings was determined by surface brightness isocontours at large radii and is not necessarily coincident with the X-ray emission peak. We prefer that azimuthal symmetry be preserved at large radii, where we are interested in characterizing profiles, at the expense of central regions.

For each instrument (i.e. MOS1 and MOS2) and each ring, we accumulated a spectrum and generated an effective area (ARF). For each observation we generated one redistribution function (RMF) for MOS1 and one for MOS2. We perform a minimal grouping to avoid channels with no counts, as required by the Cash statistic.

---

[3] A public script is available at http://xmm.esac.esa.int/external/xmm_sw_cal/background/epic_scripts.shtml

### 3.2. Spectral analysis

Spectral fitting was performed within the XSPEC v11.3 package[4]. The choice of the energy band for the spectral fitting was not trivial. We fit spectra in the 0.7−10.0 keV and in the 2.0−10.0 keV energy bands, by using the Cash statistic, with an absorbed thermal plus background model. The high-energy band has the advantage of requiring a simplified background model (see Appendices A and B); however, the bulk of source counts was excluded and the statistical quality of the measurement was substantially reduced. Due to the paucity of source counts, there is a strong degeneracy between source temperature and normalization, and the temperature is systematically underestimated; therefore, when using the 2.0−10.0 keV band, an "a posteriori" correction was required (Leccardi & Molendi 2007). In contrast, in the 0.7−10.0 keV band, the statistical quality of the data is good, but the background model is more complicated and background components are less stable and affected by strong degeneracy (see Appendices A and B). We excluded the band below 0.7 keV because the shape of the internal background is very complicated and variable with time and because the source counts reach their maximum at ≈1 keV. Hereafter, all considerations are valid for both energy bands, unless otherwise stated.

In conditions of poor statistics (i.e. few counts/bin) and high background, the Cash statistic (Cash 1979) is more suitable than the $\chi^2$ with reasonable channel grouping (Leccardi & Molendi 2007). The Cash statistic requires the number of counts in each channel to be greater than zero (Cash 1979); thus, the background cannot be subtracted. In our case the total background model is the sum of many components, each one characterized by peculiar temporal, spectral, and spatial variations (see Appendix B). When subtracting the background, the information on single components was lost. Conversely, background modeling allows one to preserve the information and to manage all components appropriately. Moreover, we recall that the background modeling does not require strong channel grouping, error propagation, or renormalization factors.

#### 3.2.1. Estimate of background parameters

To model the background, a careful characterization of all its components is mandatory. Ideally, one would like to estimate background parameters in the same region and at the same time as the source. Since this was not possible, we estimated background parameters in the external 10′−12′ ring and rescaled them in the inner rings, by making reasonable assumptions on their spatial distribution tested by analyzing blank-field observations (see Appendix B). The 10′−12′ ring often contains a weak cluster emission that, if neglected, may cause a systematic underestimate of temperature and normalization in the inner rings (see Sect. 5.1.2). In this ring the spectral components in the 0.7−10.0 keV band are:

- the thermal emission from the cluster (GCL);
- the emission from the Galaxy Halo (HALO);
- the cosmic X-ray background (CXB);
- the quiescent soft protons (QSP);
- the cosmic ray induced continuum (NXB);
- the fluorescence emission lines.

The HALO component is negligible when considering the 2.0−10.0 keV range. The model is the same one as used when analyzing blank-field observations (see Appendix B for further details) plus a thermal component for the GCL.

We fixed most parameters (namely all except for the normalization of HALO, CXB, NXB, and fluorescence lines) to reduce the degeneracy due to the presence of different components with similar spectral shapes. All cluster parameters were fixed: the temperature, $kT$, and the normalization, $N_{\rm S}$, were extrapolated from the final profiles through an iterative procedure. The metallicity, $Z$, was fixed to 0.2 solar (the solar abundances were taken from Anders & Grevesse 1989) and the redshift, $z$, was fixed to the optical value. The QSP normalization, $N_{\rm QSP}$, was calculated from $R_{\rm SB}$ (see Appendix B) and fixed. Minor discrepancies in shape or normalization with respect to the real QSP spectrum are possible, the model accounts for them by slightly changing the normalization of other components, i.e. $N_{\rm HALO}$, $N_{\rm CXB}$, and $N_{\rm NXB}$ (for the discussion of the systematic effects related to QSP see Sects. 5.1.3 and 5.2.3).

Summarizing, in the 10′−12′ ring, we have determined the range of variability, $[N_{\rm min}, N_{\rm max}]$, (i.e. the best fit value $\pm 1\sigma$ uncertainty) for the normalization of the main background components, i.e. $N_{\rm HALO}$, $N_{\rm CXB}$, and $N_{\rm NXB}$. Once properly rescaled, this information allowed us to constrain background parameters in the inner rings.

#### 3.2.2. Spectral fit in concentric rings

We fit spectra in internal rings with the same model as adopted in the 10′−12′ ring case (see Sect. 3.2.1). In Fig. 3 we compare spectra and best fit models for two different regions of the same cluster. In the inner ring (1′−1.5′) source counts dominate, while in the outer ring (4.5′−6′) background counts dominate.

The equivalent hydrogen column density along the line of sight, $N_{\rm H}$, was fixed to the 21 cm measurement (Dickey & Lockman 1990). Since clusters in our sample are at high galactic latitude ($|b| > 20°$), the $N_{\rm H}$ is $<10^{21}$ cm$^{-2}$ and the absorption effect is negligible above 1 keV. We have always left the temperature, $kT$, and the normalization, $N_{\rm S}$, free to vary. The metallicity was free below $\approx 0.4\ R_{180}$ and fixed to 0.2 solar beyond. The redshift was allowed to vary between ±7% of the optical measurement in the two innermost rings and, in the other rings, was fixed to the average value of the first two rings.

The normalization of HALO, CXB, and NXB for the inner rings were obtained by rescaling the best-fit values in the 10′−12′ ring (see Sect. 3.2.1) by the area ratio and the correction factor, $K(r)$, obtained from blank field observations (see Table B.2 in Appendix B):

$$N^{\rm int} = N^{\rm ext} \times \frac{{\rm Area}^{\rm int}}{{\rm Area}^{\rm ext}} \times K(r), \qquad (2)$$

for NXB $K = 1$ for all rings. Then, $N^{\rm int}_{\rm HALO}$, $N^{\rm int}_{\rm CXB}$, and $N^{\rm int}_{\rm NXB}$ were free to vary within a certain range: the lower (upper) limit of this range was derived by rescaling the best-fit value minus (plus) the $1\sigma$-error calculated in the 10′−12′ ring. The local background should have a variation length scale of some degrees (Snowden et al. 1997); conversely, $N_{\rm CXB}$ may have large (i.e. 20−100%) variations between different rings due to the cosmic variance. However, extensive simulations show that these statistical fluctuations do not introduce systematics in the temperature measurement, when averaging on a large sample (see Sect. 5.1.1). We obtained $N^{\rm int}_{\rm QSP}$ by rescaling the value adopted in the 10′−12′ ring by the area ratio and by the QSP vignetting profile (Kuntz 2006), and fixed it for all rings. Normalizations of instrumental fluorescence emission lines were free to vary within a limited

---

[4] `http://heasarc.nasa.gov/docs/xanadu/xspec/xspec11/index.html`

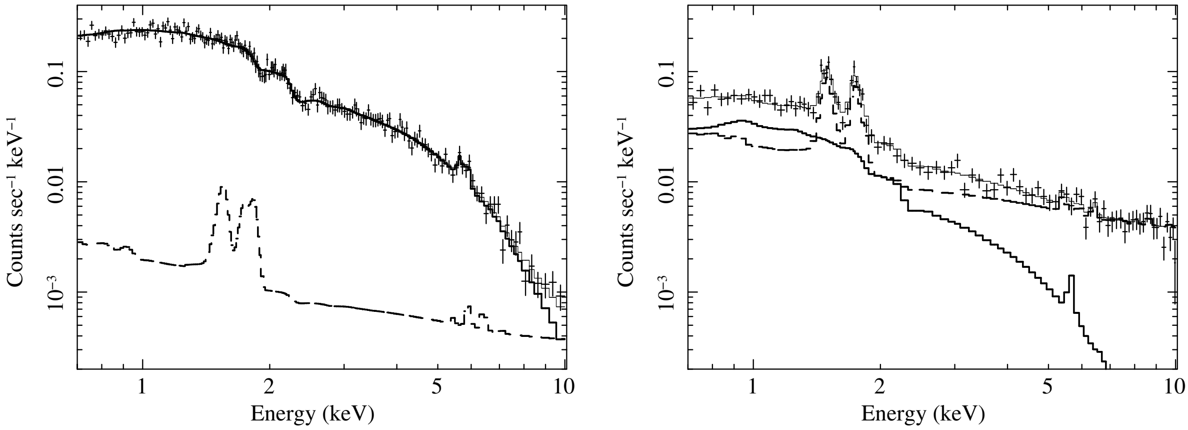

**Fig. 3.** Spectra and best fit models for the 1′−1.5′ (*left*) and the 4.5′−6′ (*right*) rings of Abell 1689. The solid thick and the dotted thick lines respectively represent the thermal and the total background model. The solid thin line represents the total (i.e. thermal + background) model. In the inner ring, source counts dominate background ones, in the outer the opposite is true.

range determined from the analysis of closed observations and have an almost negligible impact on our measurements.

For each ring, when using the 0.7−10.0 keV energy band, we determined $kT$, $Z$, and $N_S$ best fit values and one-sigma uncertainties for each MOS and calculated the weighted average. Conversely, when using the 2.0−10.0 keV band, we combined temperature measurements from different instruments as described in our previous paper (Leccardi & Molendi 2007), to correct for the bias that affects the temperature estimator. In the 0.7−10.0 keV band, there are many more source counts, the temperature estimator is much less biased, and the weighted average returns a slightly (≈3% in an outer ring) biased value (see the $F = 1.0$ case in Sect. 5.1.1).

Finally, we produced surface brightness (i.e. normalization over area), temperature, and metallicity profiles for each cluster.

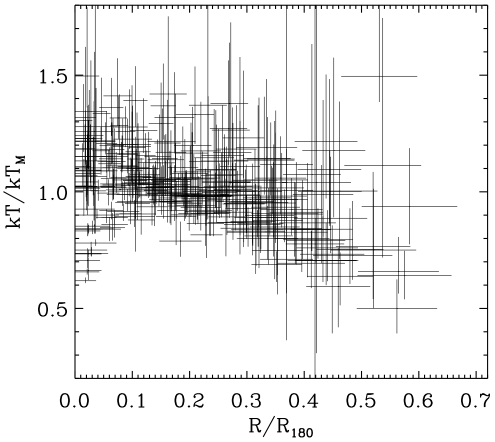

**Fig. 4.** Radial temperature profiles for all clusters in our sample rescaled by $R_{180}$ and $kT_M$.

## 4. The temperature profiles

Clusters in our sample have different temperatures and redshifts, therefore it is not trivial to identify one (or more) parameters that indicate the last ring where our temperature measurement is reliable. We define an indicator, $I$, as the source-to-background count rate ratio calculated in the energy band used for the spectral fitting. For each observation we calculated $I$ for each ring: the higher $I$, the more the source contribution, and the more reliable our measurement in this particular ring. The indicator $I$ is affected by an intrinsic bias; i.e., upward statistical fluctuations of the temperature are associated to higher $I$ (because of the difference in spectral shape between source and background models); therefore, near a threshold, the mean temperature is slightly overestimated. This systematic is almost negligible when considering the whole sample, but it may appear when analyzing a small number of objects. We note that, although present, this effect does not affect results obtained when dividing the whole sample into subsamples (e.g. Sects. 5.2.3 and 6.2).

In Fig. 4 we show the radial temperature profiles for all clusters of our sample by setting a lower limit $I_0 = 0.6$, and spectra are fitted in the 0.7−10.0 keV band. Each profile is rescaled by the cluster mean temperature, $kT_M$, computed by fitting the profile with a constant after the exclusion of the core region (i.e. for $R > 0.1\ R_{180}$). The radius is rescaled by $R_{180}$, i.e. the radius encompassing a spherical density contrast of 180 with respect to the critical density. We compute $R_{180}$ from the mean temperature and the redshift (Arnaud et al. 2005):

$$R_{180} = 1780 \left(\frac{kT_M}{5\ \mathrm{keV}}\right)^{1/2} h(z)^{-1}\ \mathrm{kpc}, \tag{3}$$

where $h(z) = (\Omega_m(1+z)^3 + \Omega_\Lambda)^{1/2}$. The scale radius, $R_{180}$, is a good approximation to the virial radius in an Einstein-De Sitter universe and has been largely used to rescale cluster radial properties (De Grandi & Molendi 2002; Vikhlinin et al. 2005). We then choose 180 as an over-density for comparing our results with previous works (see Sect. 6.6), even if the virial radius encloses a spherical density contrast of ≈100 in the current adopted cosmology (Eke et al. 1998).

The profiles show a clear decline beyond ≈0.2 $R_{180}$, and our measurements extend out to ≈0.6 $R_{180}$. The large scatter of values is mostly of statistical origin; however, a maximum likelihood test shows that, when excluding the region below 0.2 $R_{180}$, our profiles are characterized by a 6% intrinsic dispersion, which is comparable to our systematics (see Sect. 5.3), so that the existence of a universal cluster temperature profile is still an open issue. The scatter in the inner region is mostly due to the presence of both cool core and non cool core clusters, but also to our choice of preserving the azimuthal symmetry at large radii (see Sect. 3.1.3). In Fig. 5 we report temperature and radius of the

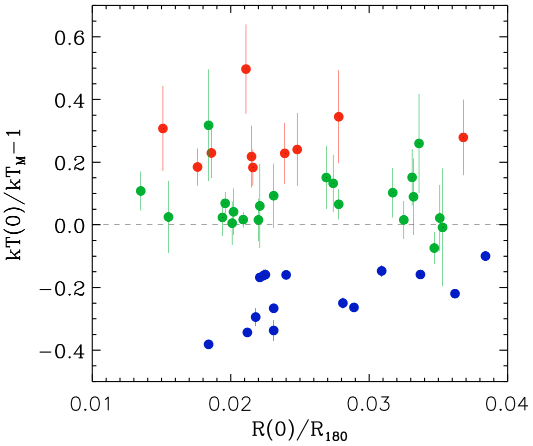

**Fig. 5.** Temperature vs. radius for the innermost ring respectively scaled by $kT_{\rm M}$ and $R_{180}$. Clusters for which the temperature is significantly (at least $3\sigma$) lower than $kT_{\rm M}$ are defined as cool cores (blue circles); those for which the temperature profile does not significantly (at least $2\sigma$) decrease are defined as non cool cores (red circles); other clusters, whose membership is not clearly determined, are classified as uncertain (green circles). When considering $z > 0.2$ clusters, which fill the right side of the panel, we expect smaller gradients due to the lower spatial resolution.

innermost ring scaled by $kT_{\rm M}$ and $R_{180}$ for all clusters. We define (i) cool core (hereafter CC) clusters as those for which the temperature is significantly (at least $3\sigma$) lower than $kT_{\rm M}$; (ii) non cool core (hereafter NCC) clusters as those for which the temperature profile does not significantly (at least $2\sigma$) decrease; and (iii) uncertain (hereafter UNC) clusters as those for which the membership is not clearly determined.

It is worth noting that the error bars are usually strongly asymmetric; i.e., the upper bar is larger than the lower. Moreover, the higher the temperature, the larger the error bars. The reason is that most of the information on the temperature is located around the energy of the exponential cut-off. Due to the spectral shapes of source and background components and to the sharp decrease of the effective areas at high energies, the source-to-background count rate ratio strongly depends on the energy band (see for example Fig. 3); i.e., the higher the cut-off energy, the lower the source-to-background ratio and the larger the uncertainties.

In Fig. 6 we report the weighted average and the scatter of all profiles shown in Fig. 4. The mean profile shows the decline beyond 0.2 $R_{180}$ more clearly. The temperature also decreases toward the center because of the presence of cool core clusters.

## 5. Evaluation of systematic effects

We carefully checked our results, searching for possible systematic effects. Prior to the analysis, we made use of extensive simulations to quantify the impact of different spectral components on a simulated temperature profile ("a priori" tests). After the analysis, we investigated how the measured temperature profile changed, when choosing different key parameters ("a posteriori" tests).

### *5.1. "A priori" tests*

We performed simulations that reproduced our analysis procedure as closely as possible. We considered two rings: the external 10′−12′, $R_{\rm ext}$, where we estimated background parameters, and the 4.5′−6′, $R_{\rm int}$, where we measured the temperature. The exposure time for each spectrum is always 20 ks, i.e. a representative value for our sample (see Fig. 2). We used the Abell 1689 EPIC-MOS1 observation as a guideline, for producing RMF and ARF, and for choosing typical input parameters. The simulation procedure is structured as follows:

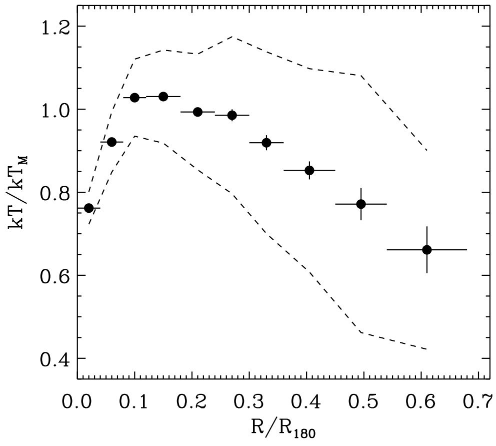

**Fig. 6.** Mean radial temperature profile rescaled by $R_{180}$ and $kT_{\rm M}$. The dotted lines show the one-sigma scatter of the values around the average.

- choice of reasonable input parameters;
- generation of 300 spectra in $R_{\rm ext}$;
- generation of 500 spectra in $R_{\rm int}$;
- estimate of background parameters in $R_{\rm ext}$;
- rescaling background parameters and fitting spectra in $R_{\rm int}$.

Simulation details are described in each section below. We tested the effect of the cosmic variance (see Sect. 5.1.1), of an inaccurate estimate of the cluster emission in $R_{\rm ext}$ (see Sect. 5.1.2), and of the QSP component (see Sect. 5.1.3). All results were obtained by fitting spectra in the 0.7−10.0 keV band. We also conducted a similar analysis for the 2.0−10.0 keV band and find that the systematics for the two bands are the same order of magnitude. We recall, however, that the hard band is characterized by the worst statistics; therefore, in this case systematic errors are masked by statistical ones and have less impact on the final measurement.

### 5.1.1. The cosmic variance

We employed a simulation to quantify the effect of the cosmic variance on temperature and normalization measurements. In this simulation we neglected the soft proton contribution; the background components are the HALO, the CXB, and the NXB, and they are modeled as for MOS1 in Appendix B. In $R_{\rm ext}$ there are only background components, while in $R_{\rm int}$ there is also the thermal source. Normalization[5] input values in $R_{\rm ext}$ are: $N^{\rm ext}_{\rm HALO} = 1.6 \times 10^{-4}$, $N^{\rm ext}_{\rm CXB} = 5.0 \times 10^{-2}$, and $N^{\rm ext}_{\rm NXB} = 1.0 \times 10^{-2}$; input values in $R_{\rm int}$ are obtained by rescaling the values in $R_{\rm ext}$ by the area ratio (i.e. as in Eq. (2) with $K(r) = 1.0$). Then, $N_{\rm CXB}$ is also multiplied by a factor, $F$, which simulates the fluctuation due to the cosmic variance between $R_{\rm int}$ and $R_{\rm ext}$. After the excision of brightest point-like sources (see Sect. 3.1.1), one-sigma fluctuations are expected to be ≈30%. We then considered 3 cases: a null ($F = 1.0$), a positive ($F = 1.3$), and a

---

[5] Normalization values are always reported in XSPEC units.

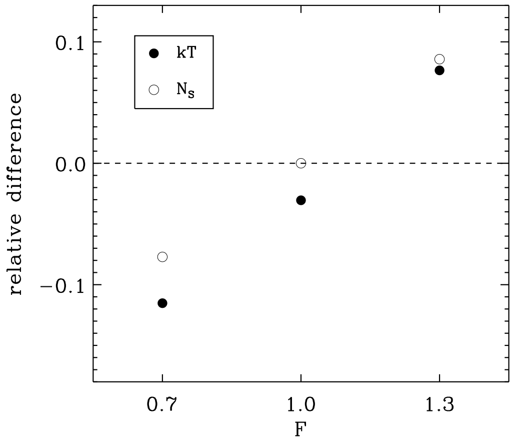

**Fig. 7.** Relative differences between measured and input values for the source temperature, $kT$, and normalization, $N_{\rm S}$, as a function of the factor $F$, which simulates the fluctuation due to the cosmic variance (see text for details). Uncertainties are smaller than the circle size. 30% fluctuations cause ≈10% variations in $kT$ and $N_{\rm S}$. For a positive/negative fluctuation, the measured $kT$ and $N_{\rm S}$ are higher/lower than the input values.

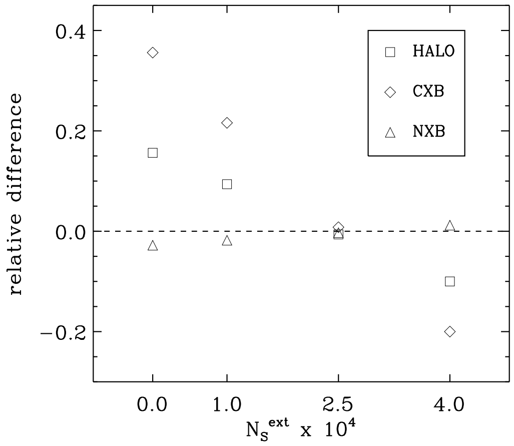

**Fig. 8.** Relative differences between measured and input values for the normalization of background components (namely $N_{\rm HALO}$, $N_{\rm CXB}$, and $N_{\rm NXB}$) as a function of the input value for cluster normalization in $R_{\rm ext}$, $N_{\rm S}^{\rm ext}$. Uncertainties are smaller than the symbol size, and $N_{\rm CXB}$ shows the strongest (negative) correlation with $N_{\rm S}^{\rm ext}$.

negative ($F = 0.7$) fluctuation. Thus, in the first case the input value for CXB in $R_{\rm int}$ is equal to that rescaled by the area ratio, in the second it is 30% higher, and in the third 30% lower. Input parameters for the thermal model in $R_{\rm int}$ are $kT = 6$ keV, $Z = 0.2\ Z_{\odot}$, $z = 0.2$, and $N_{\rm S} = 7.0 \times 10^{-4}$. In $R_{\rm ext}$, $Z$ and $z$ are fixed to the input values, while $kT$ and $N_{\rm S}$ are free. For this particular choice of the parameters, the source-to-background count rate ratio, $I$, is 1.13 (see Sect. 4). As explained in Sects. 3.2.1 and 3.2.2, we determined the ranges of variability for $N_{\rm HALO}$, $N_{\rm CXB}$, and $N_{\rm NXB}$ and rescaled them in $R_{\rm int}$. Then we fit spectra in the 0.7−10.0 keV band and calculated the weighted averages of $kT$ and $N_{\rm S}$ over the 500 simulations.

In Fig. 7 we show the relative differences between measured and input values for the temperature, $kT$ (filled circles), and the normalization, $N_{\rm S}$ (empty circles). A positive fluctuation of CXB normalization (i.e. $F = 1.3$) returns higher temperature and normalization, because the excess of counts due to the CXB is modeled by the thermal component, which is steeper than the CXB power law. For the $F = 1.0$ case, while $N_{\rm S}$ returns exactly the input value, $kT$ returns a slightly (≈3%) underestimated value, probably due to the bias on the temperature estimator (Leccardi & Molendi 2007). The effect of the cosmic variance is roughly symmetric on both $kT$ and $N_{\rm S}$, making it almost negligible when averaging over a large sample. We also performed simulations for our worst case, i.e. $I = 0.6$ (see Sect. 4), and find qualitatively the same results. For the $F = 1.0$ case, the bias on the temperature is ≈8% rather than ≈3% and the bias on the normalization is negligible.

### 5.1.2. The cluster emission in the 10′–12′ ring

The source contribution in the 10′−12′ ring, which mainly depends on cluster redshift and emission measure, is difficult to estimate with accuracy. We employed a simulation to determine how an inaccurate estimate could affect our measurement of cluster temperature, $kT$, and normalization, $N_{\rm S}$. Soft protons are neglected in this case, too; background components and their input values are the same as for the $F = 1.0$ case of the cosmic variance tests (see Sect. 5.1.1). Input parameters for the thermal model in $R_{\rm int}$ are the same as in that case, instead in $R_{\rm ext}$ are $kT^{\rm ext} = 4$ keV, $Z^{\rm ext} = 0.2\ Z_{\odot}$, $z^{\rm ext} = 0.2$, and $N_{\rm S}^{\rm ext} = 2.5 \times 10^{-4}$. For this particular choice of the parameters, the source-to-background count rate ratio, $I$, is 1.13 (see Sect. 4). When fitting spectra in $R_{\rm ext}$, all thermal parameters are fixed: namely, the temperature, the metallicity, and the redshift are fixed to the input values, while for $N_{\rm S}^{\rm ext}$ we consider 4 cases. In the first case, we neglect the source contribution ($N_{\rm S}^{\rm ext} = 0$); in the other cases, the normalization is fixed to a value lower ($N_{\rm S}^{\rm ext} = 1.0 \times 10^{-4}$), equal ($N_{\rm S}^{\rm ext} = 2.5 \times 10^{-4}$), and higher ($N_{\rm S}^{\rm ext} = 4.0 \times 10^{-4}$) than the input value. Normalizations of all background components (namely $N_{\rm HALO}$, $N_{\rm CXB}$, and $N_{\rm NXB}$) are free parameters. For each case, we computed the weighted average of $N_{\rm HALO}$, $N_{\rm CXB}$, and $N_{\rm NXB}$ over the 300 spectra in $R_{\rm ext}$ and compared them to the input values (see Fig. 8). Both $N_{\rm NXB}$ and $N_{\rm S}^{\rm ext}$ are weakly correlated; instead, $N_{\rm HALO}$ and, in particular, $N_{\rm CXB}$ show a strong negative correlation with the input value for $N_{\rm S}^{\rm ext}$, which depends on their spectral shapes. Note that, if we correctly estimate $N_{\rm S}^{\rm ext}$, then $N_{\rm HALO}$, $N_{\rm CXB}$, and $N_{\rm NXB}$ converge to their input values.

For each input value of $N_{\rm S}^{\rm ext}$ in $R_{\rm ext}$, we fit spectra in $R_{\rm int}$ in the 0.7−10.0 keV band after the usual rescaling of background parameters (see Sect. 3.2.2), calculated the weighted averages of the source temperature, $kT$, and normalization, $N_{\rm S}$, over the 500 simulations, and compared them to the input values (see Fig. 9). Values of $kT$ and $N_{\rm S}$ measured in $R_{\rm int}$ show a positive correlation with the value of $N_{\rm S}^{\rm ext}$ fixed in $R_{\rm ext}$. This is indeed expected because of the broad similarity in the spectral shapes of thermal and CXB models. In $R_{\rm ext}$ an overestimate of $N_{\rm S}^{\rm ext}$ implies an underestimate of $N_{\rm CXB}$ (see Fig. 8); $N_{\rm CXB}$ is then rescaled by the area ratio, hence underestimated in $R_{\rm int}$ too. This results in an overestimate of $kT$ and $N_{\rm S}$ in $R_{\rm int}$, as for the $F = 1.3$ case of the cosmic variance simulations (see Sect. 5.1.1). Typical uncertainties (≈50%) on $N_{\rm S}^{\rm ext}$ cause systematic 5% and 7% errors on $kT$ and $N_{\rm S}$ (see Fig. 9). Note that, after the correction for the ≈3% bias mentioned in Sect. 5.1.1, the effect on $N_{\rm S}$ and $kT$ is symmetric; thus, when averaging on a large sample, the effect on the mean profile should be almost negligible. Note also that if we were to neglect the cluster emission in the 10′−12′ ring ($N_{\rm S}^{\rm ext} = 0$), we would cause a systematic underestimate of $kT$ and $N_{\rm S}$ on the order of 7−10% (see Fig. 9).

In a real case we deal with a combination of fluctuations and cannot treat each one separately, so we employed a simulation to

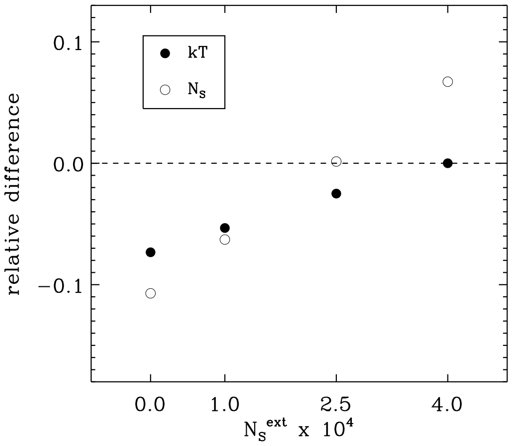

**Fig. 9.** Relative differences between measured and input values for the source temperature, $kT$, and normalization, $N_{\rm S}$, as a function of the input value for cluster normalization in $R_{\rm ext}$, $N_{\rm S}^{\rm ext}$. Uncertainties are smaller than the symbol size. An underestimate/overestimate of $N_{\rm S}^{\rm ext}$ causes $kT$ and $N_{\rm S}$ to be underestimated/overestimated.

investigate how fluctuations with different origins combine with each other. We combined effects due to the cosmic variance and to an inaccurate estimate of the cluster emission in the $10'-12'$ ring, by considering the $F = 0.7$, $F = 1.0$, and $F = 1.3$ cases mentioned in Sect. 5.1.1 and $N_{\rm S}^{\rm ext} = 1.0 \times 10^{-4}$, $N_{\rm S}^{\rm ext} = 2.5 \times 10^{-4}$, and $N_{\rm S}^{\rm ext} = 4.0 \times 10^{-4}$ mentioned in this section. The simulation procedure is the same as described before. For the cluster normalization, we find that fluctuations combine in a linear way and that effects are highly symmetric with respect to the zero case ($F = 1.0$ for the cosmic variance and $N_{\rm S}^{\rm ext} = 2.5 \times 10^{-4}$ for the cluster emission in the $10'-12'$ ring). For the cluster temperature, we find again the ≈3% bias related to the estimator; once accounted for this 3% offset, results are roughly similar to those found for the normalization case. To be more quantitative, when averaging on a large sample, the expected systematic on the temperature measurement is ≈3% due to the biased estimator and ≲2% due to deviations from the linear regime.

### 5.1.3. The QSP component

A careful characterization of the QSP component is crucial for our data analysis procedure. We employed a simulation to quantify how an incorrect estimate of the QSP contribution from the "IN over OUT" diagnostic; i.e., the $R_{\rm SB} = 1.10$ (see Sect. 3.1.2) could affect our measurements. The spectral components and their input values are the same as for the $F = 1.0$ case of the cosmic variance simulations (see Sect. 5.1.1), plus the QSP component in both rings. The model for QSP is the same as described in Appendix B. We chose two input values for $N_{\rm QSP}$ corresponding to a standard ($R_{\rm SB} = 1.10$) and a high ($R_{\rm SB} = 1.40$) level of QSP contamination. For these particular choices of the parameters, the source-to-background count rate ratio, $I$, is 1.06 for $R_{\rm SB} = 1.10$ and 0.77 for $R_{\rm SB} = 1.40$ (see Sect. 4). For each input value we considered 2 cases: an underestimate ($R_{\rm SB} = 1.05-1.35$) and an overestimate ($R_{\rm SB} = 1.15-1.45$) of the correct value. By fitting spectra in $R_{\rm ext}$ in the 0.7−10.0 keV band, we determined the range of variability of $N_{\rm HALO}$, $N_{\rm CXB}$, and $N_{\rm NXB}$, and rescaled it in $R_{\rm int}$ (see Sect. 3.2.2). We then fit spectra in $R_{\rm int}$ and compared the weighted averages of cluster temperature, $kT$, and normalization, $N_{\rm S}$, to their input values (see Fig. 10).

When considering $N_{\rm S}$, the relative difference between measured and input values is <5% for all cases and the effect is symmetric, so the impact on the mean profile obtained from a large sample should be very weak. Instead, $kT$ strongly depends on our estimate of the QSP component: the relative difference is ≈5% for $R_{\rm SB} = 1.10$ and ≈20% for $R_{\rm SB} = 1.40$. When overestimating $R_{\rm SB}$, $kT$ is underestimated, because of the broad similarity in the spectral shapes of the two components. In the $R_{\rm SB} = 1.40$ case, the values corresponding to an overestimate and an underestimate, although symmetric with respect to zero, are characterized by different uncertainties (errors in the first case are twice those in the second); thus, a weighted average returns a 10% underestimated value.

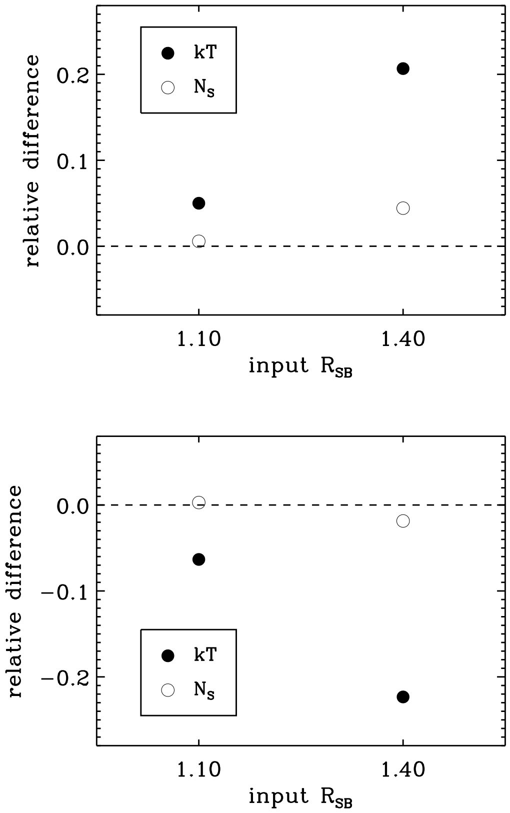

**Fig. 10.** Relative differences between measured and input values for the source temperature, $kT$, and normalization, $N_{\rm S}$, as a function of the input value for the QSP contribution, $R_{\rm SB}$. Uncertainties are smaller than the circle size. *Upper panel*: $R_{\rm SB}$ is underestimated to 1.05 and 1.35 with respect to 1.10 and 1.40. *Lower panel*: $R_{\rm SB}$ is overestimated to 1.15 and 1.45. See text for the discussion.

### 5.2. "A posteriori" tests

In this subsection we investigate how the mean profile is affected by a particular choice of key parameters: the last ring for which we measure a temperature (see Sect. 5.2.1), the energy band used for the spectral fitting (see Sect. 5.2.2), and the QSP contamination (see Sect. 5.2.3).

### 5.2.1. The truncation radius

In Sect. 4 we introduced the indicator $I$ to choose the last ring where our temperature measurement is reliable. Here we produce mean temperature profiles by averaging over all measurements for which $I > I_0$, for different values of the threshold $I_0$. In Fig. 11 we report the profiles obtained in the 0.7−10.0 keV band for different choices of $I_0$ (namely 0.0, 0.2, 0.4, 0.6, 0.8,

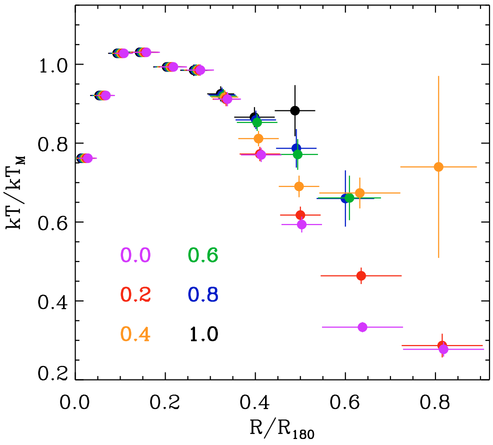

**Fig. 11.** Mean temperature profiles computed by choosing different values for the threshold $I_0$ (defined in Sect. 4) plotted with different colors. There is a clear systematic effect: the smaller the threshold, the steeper the profile. The radii have been slightly offset in the plot for clarity.

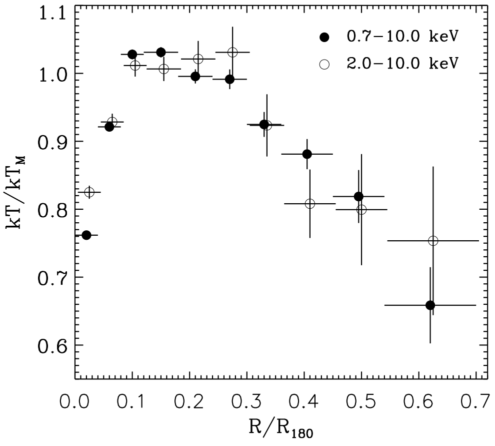

**Fig. 12.** Mean temperature profiles obtained by fitting spectra in the 0.7−10.0 keV (filled circles) and in the 2.0−10.0 keV band (empty circles). The profiles are very similar, except for the innermost point. The radii have been slightly offset in the plot for clarity.

and 1.0). As expected, the smaller the threshold, the farther the mean profile extends. If we focus on the points between 0.3 and 0.6 of $R_{180}$, we notice a clear systematic effect: the smaller the threshold, the lower the temperature. This means that, on average, the temperature is lower in those rings where the background is more important. This systematic effect becomes evident where cluster emission and background fluctuations are comparable and is probably related to small imperfections in our background modeling and to the bias on the temperature estimator (see Sect. 5.1.1). The imperfections of our background model becomes the dominant effect for low values of $I$ (namely $I \lesssim 0.4$). Thus, under a certain threshold, $I_0$, our measurements are no longer reliable. In Fig. 11 we show that $I_0 = 0.6$ represents a good compromise. Indeed, when considering the region between 0.4 and 0.5 of $R_{180}$ and comparing the average value for $kT$ obtained for a threshold $I_0 = 0.6$ and for $I_0 = 1.0$, we find a small (4% ± 3%) relative difference.

### 5.2.2. Fitting in different bands

We have fitted spectra in two different energy bands (i.e. 0.7−10.0 keV and 2.0−10.0 keV), each one characterized by different advantages and drawbacks (see Sect. 3.2). The indicator, $I$, defined in Sect. 4 depends on the band in which the count rate is calculated: more precisely, $I(0.7{-}10.0)$ is roughly 1.5 times greater than $I(2.0{-}10.0)$ for low values (i.e. $I \lesssim 2.0$). The threshold $I_0 = 0.6$ in the 0.7−10.0 keV band corresponds to $I_0 = 0.4$ in the 2.0−10.0 keV band (see Sect. 5.2.1). In Fig. 12 we compare the mean temperature profile obtained in the 0.7−10.0 keV band ($I_0 = 0.6$) with the one obtained in the 2.0−10.0 keV band ($I_0 = 0.4$). The profiles are very similar, except for the innermost point. The uncertainties in the 0.7−10.0 case are much smaller at all radii, even if the total number of points (i.e. the number of rings for all cluster) is the same, because the higher statistics at low energies allows a substantial reduction of the errors on single measurements.

In the most internal point, a high discrepancy between the two measurements is present, although in that region the background is negligible. This is due to the superposition, along the line of sight, of photons emitted by optically thin ICM with different densities and temperatures. When looking at the center of cool core clusters, the line of sight intercepts regions characterized by strong temperature gradients, so the accumulated spectrum is the sum of many components at different temperatures. In this case, the best fit value for the temperature strongly depends on the energy band (i.e. the harder the band, the higher the temperature), because the exclusion of the soft band implies the exclusion of most of the emission from cooler components (Mazzotta et al. 2004).

### 5.2.3. Contamination from QSP

We divided clusters in our sample into four groups, according to the QSP contamination that we estimate from $R_{\rm SB}$ (see Sect. 3.1.2). In Fig. 13 we report the mean temperature profiles for the four groups, by fitting spectra in the 0.7−10.0 keV band and fixing $I_0 = 0.6$. When dividing clusters into subsamples, we chose larger bin sizes to reduce the error bars. When $R_{\rm SB}$ was high, our selection criterion based on the source-to-background count rate ratio (see Sects. 4 and 5.2.1) excluded the outer rings, indeed the red profile only extends out to 0.5 $R_{180}$. No correlation is found between the shape of the profiles and $R_{\rm SB}$; i.e., the four profiles are fully consistent. The discrepancy in the innermost ring is due to the presence of a different number of cool core clusters in each group. We therefore conclude that the systematic error associated to the QSP contamination is smaller than statistical errors (≈7% beyond 0.4 $R_{180}$).

## 5.3. *A budget for systematics*

In this subsection we summarize the main results for what concern systematic errors associated to our mean profile. We compare expected systematics computed from “a priori” tests with measured systematics from “a posteriori” tests.

The $F = 1.0$ case in Sect. 5.1.1 and the $N_{\rm S}^{\rm ext} = 2.5 \times 10^{-4}$ case in Sect. 5.1.2 show that our analysis procedure is affected by a 3% to 8% systematic underestimate of the temperature when analyzing the outermost rings. The bias is probably related to the temperature estimator as described in Leccardi & Molendi (2007). In contrast, the normalization estimator is unbiased. In Sects. 5.1.1 and 5.1.2, we also found that the effects of the cosmic variance and of an inaccurate estimate of the cluster emission in the external ring are symmetric for both the temperature, $kT$, and the normalization, $N_{\rm S}$. In Sect. 5.1.2 we found that the effects due to fluctuations with different origins combine in

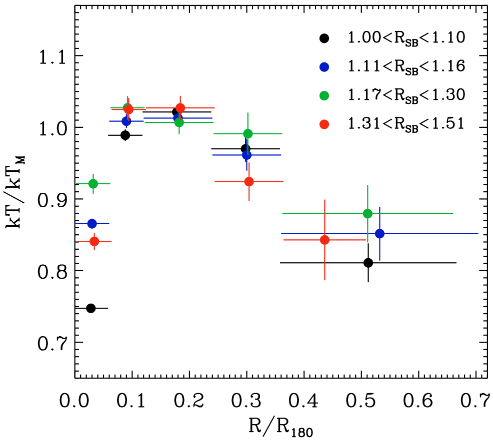

**Fig. 13.** Mean temperature profiles as a function of the QSP contamination, $R_{\mathrm{SB}}$. The four profiles are fully consistent, and no correlation is found between the shape of the profiles and $R_{\mathrm{SB}}$. The radii have been slightly offset in the plot for clarity.

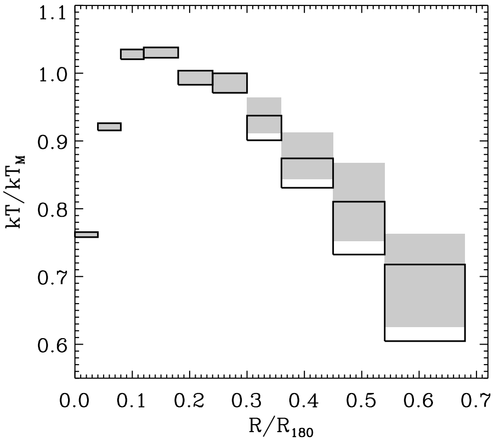

**Fig. 14.** Mean temperature profile rescaled by $R_{180}$ and $kT_{\mathrm{M}}$. For each ring, empty boxes and shaded regions indicate one-sigma uncertainties respectively before and after the bias correction.

a linear way and, when averaging over a large sample, the systematic associated to the mean profile is almost negligible for $N_{\mathrm{S}}$ and $\lesssim 2\%$ for $kT$. Thus, the expected systematic for $kT$ is $\lesssim 5\%$.

In Sect. 5.1.3 we found that, for a standard level of contamination ($R_{\mathrm{SB}} = 1.10$), a typical 5% error in the estimate of $R_{\mathrm{SB}}$ causes negligible effects on both measurements of cluster temperature and normalization. The same error causes negligible effects on $N_{\mathrm{S}}$ measurements for a high level of contamination ($R_{\mathrm{SB}} = 1.40$). In contrast, effects on $kT$ for $R_{\mathrm{SB}} = 1.40$ are important: the same 5% error causes a 10% underestimate of $kT$, also when averaging over a large sample. However, at the end of Sect. 5.2.3, in particular from Fig. 13, we have concluded that, when considering the whole sample, the systematic error associated to the QSP contamination is smaller than statistical errors ($\approx 7\%$ beyond 0.4 $R_{180}$). The difference between expected and measured systematic errors is only apparent. Indeed, when analyzing our sample, we averaged measurements that span a wide range of values for $R_{\mathrm{SB}}$ and $I$; conversely, the 10% systematic error is expected for an unfavorable case, i.e. $R_{\mathrm{SB}} = 1.40$ and $I = 0.77$ (see Sect. 5.1.3).

In Sect. 5.2.1 we compared the mean temperature value obtained for a threshold $I_0 = 0.6$ and for $I_0 = 1.0$ in an outer region (i.e. between 0.4 and 0.5 of $R_{180}$). In this ring the mean value for the indicator $I$ is 1.14, thus the expected bias related to the temperature estimator is $\approx 3\%$ (see Sect. 5.1.1). We measured a 4% ± 3% temperature discrepancy, which is consistent with the expected bias. As pointed out in Sect. 5.2.1, the discrepancy could also be due to small imperfections in our background model. We are not able to quantify the amount of this contribution, but we expect it to be small when considering $I > 0.6$.

To summarize, in external regions our measurements of the cluster temperature are affected by systematic effects, which depend on the radius through the factor $I$, i.e. the source-to-background count rate ratio. For each ring, we calculated the mean value for $I$, estimated the expected bias from simulations, and applied a correction to our mean profile. The expected bias is negligible for internal rings out to 0.30 $R_{180}$ (for which $I \gtrsim 3$), is 2–3% for 0.30–0.36 and 0.36–0.45 bins, and is $\approx 5\%$ for the last two bins (i.e. 0.45–0.54 and 0.54–0.70). We associate to our correction an uncertainty close to the correction itself, accounting for our limited knowledge from our "a posteriori" tests of the precise value of the bias. In Fig. 14 we show the mean temperature profile before and after the correction for the bias.

**Table 4.** Mean temperature values rescaled by $kT_{\mathrm{M}}$ and corrected for the biases discussed in the text, for each interval in units of $R_{180}$.

| Ring[a] | Temperature[b] |
|---|---|
| 0.00–0.04 | 0.762 ± 0.004 |
| 0.04–0.08 | 0.921 ± 0.005 |
| 0.08–0.12 | 1.028 ± 0.007 |
| 0.12–0.18 | 1.030 ± 0.008 |
| 0.18–0.24 | 0.993 ± 0.010 |
| 0.24–0.30 | 0.985 ± 0.014 |
| 0.30–0.36 | 0.938 ± 0.026 |
| 0.36–0.45 | 0.878 ± 0.035 |
| 0.45–0.54 | 0.810 ± 0.058 |
| 0.54–0.70 | 0.694 ± 0.069 |

Notes. [a] In units of $R_{180}$; [b] in units of $kT_{\mathrm{M}}$.

In Table 4 we report the corrected values for each bin. The uncertainty is the quadrature sum of the statistical error and of the error associated to our correction. Hereafter, we will consider the mean profile corrected for the bias, unless otherwise stated. Note that the bias is always comparable to the statistical uncertainties. For this reason, ours can be considered as a definitive work, for what concerns the measurement of radial temperature profiles of galaxy clusters with *XMM-Newton*. We have reached the limits imposed by the instrument and by the analysis technique, so that increasing of the number of objects will not improve the quality of the measurement.

## 6. The mean temperature profile

### 6.1. Characterizing the profile

We fit profiles (see Fig. 4) beyond 0.2 $R_{180}$ with a linear model and a power law to characterize the profile decline. By using a linear model

$$\frac{kT}{kT_{\mathrm{M}}} = A - B\left(\frac{R}{R_{180}} - 0.2\right), \tag{4}$$

we find $A = 1.02 \pm 0.01$ and $B = 0.77 \pm 0.11$. By using a power law

$$\frac{kT}{kT_{\mathrm{M}}} = N\left(\frac{R}{0.2\,R_{180}}\right)^{-\mu}, \tag{5}$$

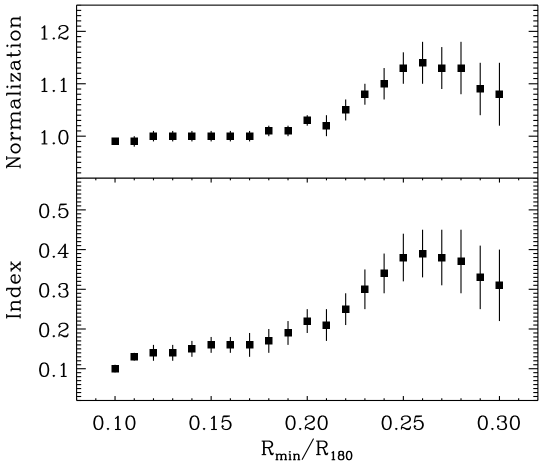

**Fig. 15.** Power-law best-fit parameters obtained by fitting profiles beyond a variable radius, $R_{\min}$, in units of $R_{180}$. The normalization is calculated at 0.2. The index best-fit value is not constant with $R_{\min}$, thus the ICM cannot be considered as a polytrope.

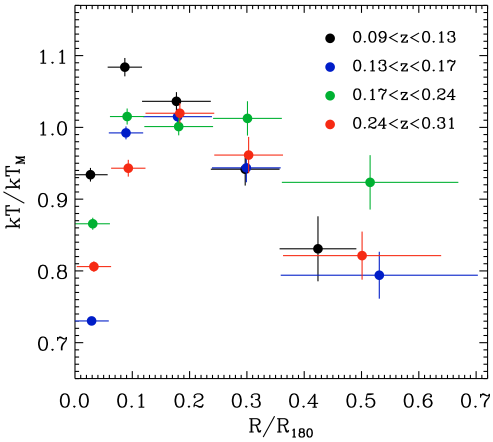

**Fig. 16.** Mean temperature profiles for the four $z$-binned groups of clusters. There is no indication of profile evolution. The radii have been slightly offset in the plot for clarity.

we find $N = 1.03 \pm 0.01$ and $\mu = 0.24 \pm 0.04$. If the gas can be approximated by a polytrope, we can derive its index, $\gamma$, from the slope of projected temperature profiles, $\mu$ (De Grandi & Molendi 2002):

$$\gamma = 1 + \mu/2, \tag{6}$$

under the assumption that, at large radii, three-dimensional gas temperature and density profiles be well described, respectively, by a power law and a $\beta$-model with $\beta = 2/3$. For $R > 0.2\ R_{180}$, we measure $\gamma = 1.12 \pm 0.02$, which is an intermediate value between those associated to isothermal ($\gamma = 1.0$) and adiabatic ($\gamma = 1.67$) gas. However, we note that the power-law best-fit parameters depend on the chosen region (see Fig. 15), as well as the derived $\gamma$, thus the above values should be taken with some caution.

### *6.2. Redshift evolution*

We divide our clusters into four groups according to the redshift, to investigate a possible evolution of temperature profiles with cosmic time. In Fig. 16 we report the mean temperature profiles for the four groups. Spectra are fitted in the 0.7–10.0 keV band and $I_0 = 0.6$ (see Sect. 4). As in the following Sects. 6.3 and 6.4, when dividing clusters into subsamples, the profiles are not corrected for biases (see Sect. 5.3), because when comparing subsamples we are not interested in determining the absolute value of the temperature, but in searching for relative differences. Moreover, in Figs. 16 and 18 we choose larger bin sizes to reduce the error bars (as in Fig. 10). The four profiles are very similar: the discrepancy in the outer regions is comparable to statistical and systematic errors, and the difference in the central region is due to a different fraction of cool core clusters. We fit each group of profiles with a power law beyond 0.2 $R_{180}$ and report results in Fig. 17. Since there is no clear correlation between the two parameters and the redshift, we conclude from the analysis of our sample that there is no indication of profile evolution up to $z = 0.3$.

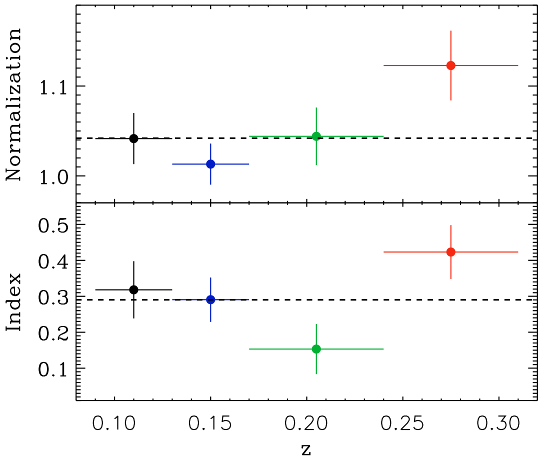

**Fig. 17.** Best fit parameters obtained by fitting each group of profiles with a power law beyond 0.2 $R_{180}$. The normalization is calculated at 0.2 $R_{180}$. The dashed lines indicate the best fit values for the whole sample. No clear correlation is found between power-law parameters and the redshift.

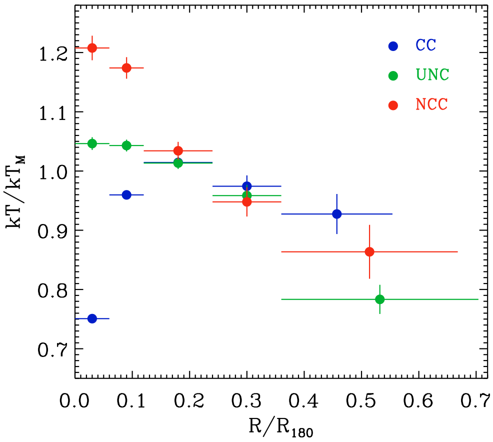

**Fig. 18.** Mean temperature profiles for cool core (blue), non cool core (red), and uncertain (green) clusters. Profiles differ by definition in the core region and are consistent in the outer regions.

### *6.3. Cool core and non cool core clusters*

In Sect. 4 we defined three groups: clusters that clearly host a cool core, clusters with no evidence of a cool core, and uncertain clusters. In Fig. 18 we show mean temperature profiles for the three groups. Spectra are fitted in the 0.7–10.0 keV band and

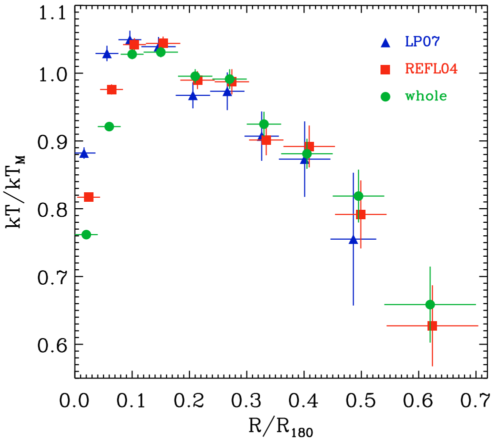

**Fig. 19.** Mean temperature profiles obtained from the LP07 subsample (blue triangles), the REFL04 subsample (red squares), and the whole sample (green circles). The three profiles are fully consistent in the outer regions. The radii have been slightly offset in the plot for clarity.

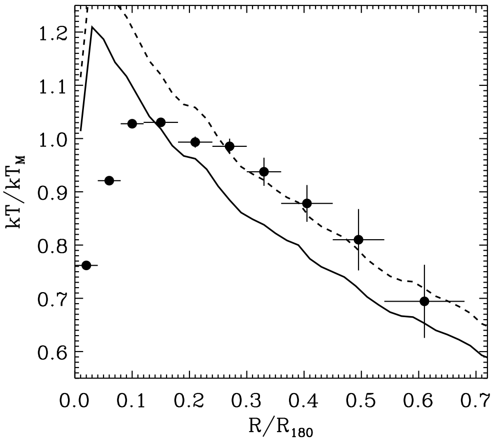

**Fig. 20.** Comparison between our observed mean profile (circles) and the one derived from hydrodynamic simulations (Borgani et al. 2004) by averaging over clusters with $kT > 3$ keV (solid line). The dashed line is obtained by rescaling the solid one by 10%.

$I_0 = 0.6$. Profiles differ by definition in the core region and are consistent beyond ≈0.1 $R_{180}$.

### 6.4. REFL04 and LP07 subsamples

Our sample is not complete with respect to any property. However, most of our clusters (≈2/3) belong to the REFLEX Cluster Survey catalog (Böhringer et al. 2004), a statistically complete X-ray flux-limited sample of 447 galaxy clusters, and a dozen objects belong to the *XMM-Newton* Legacy Project sample (Pratt et al. 2007), which is representative of an X-ray flux-limited sample with $z < 0.2$ and $kT > 2$ keV. We then selected two subsamples from our sample: clusters that belong to the REFLEX catalog (REFL04 subsample) and to the Legacy Project sample (LP07 subsample). The smaller (i.e. the LP07) is derived from Pratt's parent sample, by applying our selection criteria based on cluster temperature and redshift. We also excluded cluster observations that are heavily affected by soft proton contamination; however, the latter selection should be equivalent to a random choice and introduce no bias. Thus, we expect the LP07 subsample to be representative of an X-ray flux-limited sample of galaxy clusters with $0.1 < z < 0.2$ and $kT > 3.3$ keV. The larger (i.e. the REFL04) subsample includes the LP07 one. Clusters that belong to the REFL04, but not to the LP07, were observed with *XMM-Newton* for different reasons. They are not part of a large program and almost all observations have different PIs. Thus, there are no obvious reasons to believe that the sample is significantly biased with respect to any fundamental cluster property. A similar reasoning leads to the same conclusion for our whole sample.

In Fig. 19 we compare mean temperature profiles obtained from the two subsamples and the whole sample. The three profiles are fully consistent beyond ≈0.1 $R_{180}$, the difference in the central region is due to a different fraction of CC clusters. These results allow us to conclude that our whole sample is representative of hot, intermediate redshift clusters with respect to temperature profiles, i.e. the quantity we are interested in.

### 6.5. Comparison with hydrodynamic simulations

In this subsection we compare our mean temperature profile with the one derived from cluster hydrodynamic simulations by Borgani et al. (2004, hereafter B04). The authors used the TREE+SPH code GADGET (Springel et al. 2001) to simulate a concordance cold dark-matter cosmological model ($\Omega_{\rm m} = 0.3$, $\Omega_\Lambda = 0.7$, $\sigma_8 = 0.8$, and $h = 0.7$) within a box of 192 $h^{-1}$ Mpc on a side, $480^3$ dark-matter particles, and as many gas particles. The simulation includes radiative cooling, star formation, and supernova feedback. Simulated cluster profiles are scaled by the emission-weighted global temperature and $R_{180}$ calculated from its definition (i.e. the radius encompassing a spherical density contrast of 180 with respect to the critical density). In Fig. 20 we compare our observed profile to the projected mean profile obtained by averaging over simulated clusters with $kT > 3$ keV. The evident mismatch between the two profiles is most likely due to a different definition for the scaling temperature: actually, it is known that the emission weighted temperature is higher than the mean temperature obtained from observational data (Mazzotta et al. 2004). By rescaling the B04 profile by 10%, we find good agreement between simulation and our data beyond ≈0.25 $R_{180}$. Conversely in the core region, simulations are not able to reproduce the observed profile shape.

### 6.6. Comparison with previous observations

In this section we compare our mean temperature profile (LM08) with those obtained by other authors, namely De Grandi & Molendi (2002), Vikhlinin et al. (2005), and Pratt et al. (2007). De Grandi & Molendi (DM02) have analyzed a sample of 21 hot ($kT > 3.3$ keV), nearby ($z \lesssim 0.1$) galaxy clusters observed with *BeppoSAX*. Their sample includes both CC and NCC clusters. Vikhlinin et al. (V05) analyzed a sample of 13 nearby ($z \lesssim 0.2$), relaxed galaxy clusters and groups observed with *Chandra*. We selected from their sample only the hottest ($kT > 3.3$ keV) 8 clusters, for a more appropriate comparison with our sample. Pratt et al. (P07) analyzed a sample of 15 hot ($kT > 2.8$ keV), nearby ($z \lesssim 0.2$) clusters observed with *XMM-Newton*. Clusters of their sample present a variety of X-ray morphology.

Comparing different works is not trivial. Cluster physical properties, instrumental characteristics, and data analysis procedures may differ. Moreover, each author uses his own recipe to calculate a mean temperature and to derive a scale radius. We rescaled temperature profiles obtained by other authors by using the standard cosmology (see Sect. 1) and calculating the mean temperature, $kT_{\rm M}$, and the scale radius, $R_{180}$, as explained

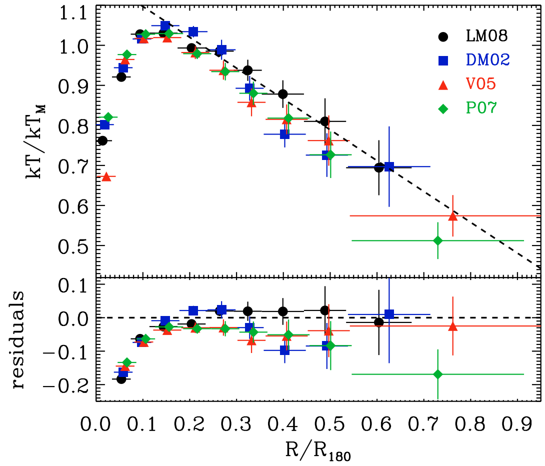

**Fig. 21.** *Upper panel*: mean temperature profiles obtained from this work (black circles, LM08), by De Grandi & Molendi (blue squares, DM02), by Vikhlinin et al. (red upward triangles, V05), and by Pratt et al. (green diamonds, P07). All profiles are rescaled by $kT_M$ and $R_{180}$ as defined in Sect. 4. The dashed line shows the best fit with a linear model beyond 0.2 $R_{180}$ (see Sect. 6.1) and is drawn to guide the eye. *Lower panel*: residuals with respect to the linear model. The LM08 profile is the flattest one.

in Sect. 4; the aim is to reduce all inhomogeneities as much as possible.

In Fig. 21 we compare the four mean temperature profiles, rescaled by $kT_M$ and $R_{180}$. Due to the correction for the biases described in Sect. 5.3, our mean profile is somewhat flatter than others beyond ≈0.2 $R_{180}$. Discrepancies in the core region are due to a different fraction of CC clusters. The outermost point of the P07 profile is ≈25% lower; however, it is only constrained by two measurements beyond ≈0.6 $R_{180}$. Our indicator, $I$, (see Sect. 4) warns about the reliability of these two measurements, for which $I \approx 0.3$, i.e. a half of our threshold, $I_0 = 0.6$. In Fig. 11 we show that, when using our analysis technique, lower values of $I$ are associated to a bias on the temperature measurement. We assume that a somewhat similar systematic may affect the P07 analysis technique, too. When excluding these two measurements, the P07 mean profile only extends out to ≈0.6 $R_{180}$ and is consistent with ours (see also Fig. 22). It is possible that measurements obtained with other experiments be also affected by a similar kind of systematics, which make the profiles steeper.

We fit observed and simulated cluster profiles with a power law beyond 0.2 $R_{180}$ and in Fig. 22 report best fit parameters. The LM08 profile is the flattest one; however, all observed profile indices are consistent within 2−3 sigma. In Sect. 5.3 we have quantified the systematic underestimate on the temperature measurement associated to our procedure. Since it depends on the indicator $I$, which itself depends on the radius, we also expect a net effect on the profile index, $\mu$; namely, we expect $\mu$ to be overestimated. For this reason, it is possible that the discrepancy between indices obtained from different works (reported in Fig. 22) may not have a purely statistical origin. We calculate an average profile index, $\mu = 0.31 \pm 0.02$, which is significantly lower than obtained from the B04 profile, $\mu = 0.39$; however, for the simulation we are not able to provide an estimate of parameter uncertainty.

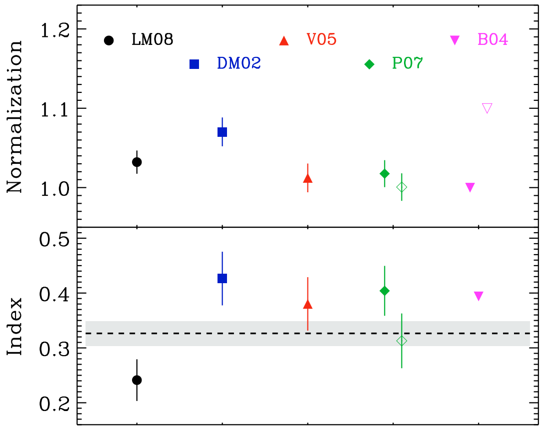

**Fig. 22.** Best fit parameters, obtained by fitting observed and simulated cluster profiles with a power law, beyond 0.2 $R_{180}$. In *the upper panel* we report the normalization, in the lower the index. We use the same symbols as in Fig. 21 for observed clusters and a violet downward triangle for Borgani's work (B04). The normalization is calculated at 0.2 $R_{180}$. For P07 we report two values, empty diamonds indicate index and normalization obtained when excluding the two outermost measurements (see text for details). The empty downward triangle indicates the normalization of the B04 rescaled profile (see Sect. 6.5). In *the lower panel*, the dashed line and the shaded region represent the weighted average and its one sigma confidence interval derived from the observed profiles only (for P07 we use the lower value, i.e. the empty diamond). As previously noted from Fig. 21, the LM08 profile is the flattest one, but all indices of observed profiles are consistent within two sigma. Conversely, the B04 profile seems to be significantly steeper, but in this case we are not able to provide an estimate of parameter uncertainty.

## 7. Summary and conclusions

We have analyzed a sample of ≈50 hot, intermediate redshift galaxy clusters (see Sect. 2) to measure their radial properties. In this paper we focused on the temperature profiles and postponed the analysis of the metallicity to a forthcoming paper (Leccardi & Molendi 2008, submitted). In Sect. 6.4 we showed that our sample should be representative of hot, intermediate redshift clusters, at least with respect to the temperature profile.

Our main results are summarized as follows.

- The mean temperature profile declines with radius in the 0.2 $R_{180}$−0.6 $R_{180}$ range (see Sect. 4).
- When excluding the core region, the profiles are characterized by an intrinsic dispersion (6%) comparable to the estimated systematics, (see Sect. 4).
- There is no evidence of profile evolution with redshift out to $z \approx 0.3$ (see Sect. 6.2).
- The profile slope in the outer regions is independent of the presence of a cool core (see Sect. 6.3).
- The slope of our mean profile is broadly similar to those obtained from hydrodynamic simulations. We find a discrepancy of ≈10% in normalization probably due to a different definition for the scaling temperature (see Sect. 6.5).
- When compared to previous works, our profile is somewhat flatter (see Sect. 6.5), probably due to a different level of characterization of systematic effects, which become very important in the outer regions.

The above results were obtained using a novel data analysis technique, which includes two major improvements. First, we used the background modeling, rather than the background subtraction, and the Cash statistic rather than the $\chi^2$. This method requires a careful characterization of all background components. Second, we assessed systematic effects in detail. We performed two groups of tests to quantify the impact of different components on simulated spectra, and to investigate how the measured temperature profile changes when choosing different key parameters.

Our work not only provides a confirmation of previous results. For the first time, we believe we know where the systematics come from and how large they are. Indeed, this work allows us to not only constrain cluster temperature profiles with confidence in the outer regions, but also, from a more general point of view, to explore the limits of the current X-ray experiments (in particular *XMM-Newton*). It is crucial that we learn how best to exploit *XMM-Newton* data, because for the next 5−10 years there will be no experiments with comparable or improved capabilities, as far as low surface-brightness emission is concerned. Our work will also allow us to look forward to ambitious new measurements: an example is the attempt to measure the putative shock in Abell 754, for which we have obtained a ≈200 ks observation with *XMM-Newton* in AO7.

*Acknowledgements.* We acknowledge the financial contribution from contracts ASI-INAF I/023/05/0 and I/088/06/0. We thank S. Ghizzardi, M. Rossetti, and S. De Grandi for a careful reading of the manuscript. We thank S. Borgani, G. W. Pratt, and A. Vikhlinin for kindly providing their temperature profiles.

## References

Anders, E., & Grevesse, N. 1989, Geochim. Cosmochim. Acta, 53, 197
Arnaud, M., Pointecouteau, E., & Pratt, G. W. 2005, A&A, 441, 893
Böhringer, H., Schuecker, P., Guzzo, L., et al. 2004, A&A, 425, 367
Borgani, S., Murante, G., Springel, V., et al. 2004, MNRAS, 348, 1078
Cash, W. 1979, ApJ, 228, 939
De Grandi, S., & Molendi, S. 2002, ApJ, 567, 163
De Luca, A., & Molendi, S. 2004, A&A, 419, 837
Dickey, J. M., & Lockman, F. J. 1990, ARA&A, 28, 215
Eke, V. R., Navarro, J. F., & Frenk, C. S. 1998, ApJ, 503, 569
Ettori, S., De Grandi, S., & Molendi, S. 2002, A&A, 391, 841
Fabian, A. C., & Allen, S. W. 2003, in Texas in Tuscany, XXI Symposium on Relativistic Astrophysics, ed. R. Bandiera, R. Maiolino, & F. Mannucci, 197
Finoguenov, A., Arnaud, M., & David, L. P. 2001, ApJ, 555, 191
Henry, J. P., & Arnaud, K. A. 1991, ApJ, 372, 410
Irwin, J. A., & Bregman, J. N. 2000, ApJ, 538, 543
Irwin, J. A., Bregman, J. N., & Evrard, A. E. 1999, ApJ, 519, 518
Keith, H. D., & Loomis, T. C. 1978, X-ray spectrometry, 7, 217
Kuntz, K. 2006 `ftp://epic3.xra.le.ac.uk/pub/cal-pv/meetings/mpe-2006-05/kk.pdf`
Kuntz, K. D., & Snowden, S. L. 2000, ApJ, 543, 195
Leccardi, A., & Molendi, S. 2007, A&A, 472, 21
Markevitch, M., Forman, W. R., Sarazin, C. L., & Vikhlinin, A. 1998, ApJ, 503, 77
Mazzotta, P., Rasia, E., Moscardini, L., & Tormen, G. 2004, MNRAS, 354, 10
McCarthy, I. G., Balogh, M. L., Babul, A., Poole, G. B., & Horner, D. J. 2004, ApJ, 613, 811
McNamara, B. R., Nulsen, P. E. J., Wise, M. W., et al. 2005, Nature, 433, 45
Piffaretti, R., Jetzer, P., Kaastra, J. S., & Tamura, T. 2005, A&A, 433, 101
Ponman, T. J., Sanderson, A. J. R., & Finoguenov, A. 2003, MNRAS, 343, 331
Pratt, G. W., Arnaud, M., & Pointecouteau, E. 2006, A&A, 446, 429
Pratt, G. W., Böhringer, H., Croston, J. H., et al. 2007, A&A, 461, 71
Roncarelli, M., Ettori, S., Dolag, K., et al. 2006, MNRAS, 373, 1339
Snowden, S. L., Egger, R., Freyberg, M. J., et al. 1997, ApJ, 485, 125
Snowden, S. L., Mushotzky, R. F., Kuntz, K. D., & Davis, D. S. 2008, A&A, 478, 615
Springel, V., Yoshida, N., & White, S. D. M. 2001, New Astron., 6, 79
Tozzi, P., Scharf, C., & Norman, C. 2000, ApJ, 542, 106
Vikhlinin, A., Markevitch, M., Murray, S. S., et al. 2005, ApJ, 628, 655
Voit, G. M. 2005, Adv. Space Res., 36, 701
White, D. A. 2000, MNRAS, 312, 663

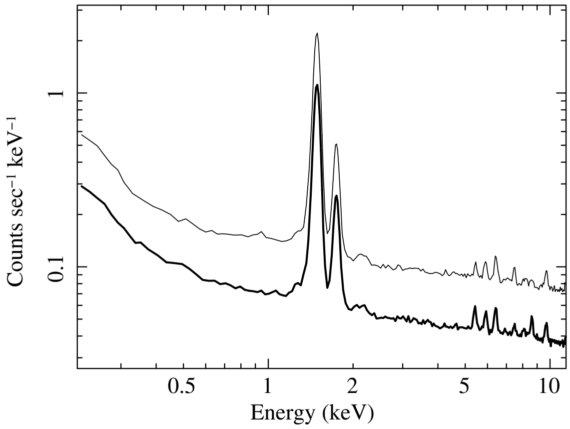

**Fig. A.1.** MOS1 (thick) and MOS2 (thin) spectra from closed observations in the whole energy band, i.e. 0.2−11.3 keV. MOS2 spectrum is scaled by a factor of 2 for clarity. Spectra were accumulated in the 10′−12′ ring. The total exposure time is ≈650 ks.

**Table A.1.** Best fit parameters for the NXB broken power law. $\Gamma_1$ and $\Gamma_2$ are the slopes below and above the break energy, $E_B$.

| | $\Gamma_1$ | $E_B$ [keV] | $\Gamma_2$ |
|---|---|---|---|
| MOS1 | 0.22 | 7.0 | 0.05 |
| MOS2 | 0.32 | 3.0 | 0.22 |

## Appendix A: The analysis of "closed" observations

We analyzed a large number (≈50) of observations with the filter wheel in the "closed" position to characterize the EPIC-MOS internal background in detail and to provide constraints to the background model, which we use for analyzing our data. Exposure times of individual observations cover between 5 and 100 ks for a total exposure time of ≈650 ks.

For each observation, we selected 6 concentric rings (0′−2.75′, 2.75′−4.5′, 4.5′−6′, 6′−8′, 8′−10′, and 10′−12′) centered on the detector center. For each instrument (i.e. MOS1 and MOS2) and each ring, we produced the total spectrum by summing, channel by channel, spectral counts accumulated during all observations. We associated the appropriate RMF to each total spectrum and performed a minimal grouping to avoid channels with no counts. In Fig. A.1 we report the total spectra accumulated in the 10′−12′ ring, for MOS1 and MOS2, in the 0.2−11.3 keV band. Closed observation events are solely due to the internal background, which is characterized by a cosmic-ray induced continuum (NXB) plus several fluorescence emission lines. The most intense lines are due to Al (≈1.5 keV) and Si (≈1.8 keV). Beyond 2 keV we fit the NXB with a single power law (index 0.24 and 0.23 for MOS1 and MOS2 respectively); instead, for the 0.7−10.0 keV range, a broken power-law (see Table A.1) was more appropriate. Emission lines were modeled by Gaussians. Note that particle background components were not multiplied by the effective area.

In Table A.2 we list the emission lines of our model with their rest frame energies. Normalization values are always reported in XSPEC units. Lines are determined by 3 parameters: peak energy, intrinsic width and normalization. The energy of Al K$\alpha$, $E_{\rm Al}$, was free to allow for a small shift in the energy scale; the energies of Al, Si, and Au-M lines were linked to $E_{\rm Al}$ in such a way that a common shift, $\Delta E$, was applied to all lines. Similarly, the energy of Cr K$\alpha$, $E_{\rm Cr}$, was free and the energies of all other lines were linked to $E_{\rm Cr}$. The intrinsic width was always fixed to zero, except for Al and Si lines for which it was fixed to 0.0022 keV to allow for minor mismatches in energy calibrations for different observations. Normalizations of K$\alpha$, Al, and Si lines were free, while normalizations of K$\beta$ lines were forced to be one seventh of the correspondent K$\alpha$ line (Keith & Loomis 1978). The correlation between broken power-law and Gaussian parameters is very weak.

**Table A.2.** Instrumental emission lines in the 0.7−10.0 keV energy band.

| Line | $E$ [keV] | Line | $E$ [keV] |
|---|---|---|---|
| Al K$\alpha$ | 1.487 | Mn K$\beta$ | 6.490 |
| Al K$\beta$ | 1.557 | Fe K$\beta$ | 7.058 |
| Si K$\alpha$ | 1.740 | Ni K$\alpha$ | 7.472 |
| Si K$\beta$ | 1.836 | Cu K$\alpha$ | 8.041 |
| Au M$\alpha$ | 2.110 | Ni K$\beta$ | 8.265 |
| Au M$\beta$ | 2.200 | Zn K$\alpha$ | 8.631 |
| Cr K$\alpha$ | 5.412 | Cu K$\beta$ | 8.905 |
| Mn K$\alpha$ | 5.895 | Zn K$\beta$ | 9.572 |
| Cr K$\beta$ | 5.947 | Au L$\alpha$ | 9.685 |
| Fe K$\alpha$ | 6.400 | | |

As noticed by Kuntz (2006), there are observations in which the count rate of some CCDs is very different, especially at low energies, indicating that the NXB spectral shape is not constant over the detector. In particular, this problem affects MOS1 CCD-4 and CCD-5 and MOS2 CCD-2 and CCD-5. Since our procedure requires background parameters to be rescaled from the outer to the inner rings, we always excluded the above mentioned "bright" CCDs from data analysis when using the 0.7−10.0 keV band (see Sect. 3.1.1). This was not necessary when using the band above 2 keV, because the effect is negligible for almost all observations.

After the exclusion of the bright CCDs, we fit spectra accumulated in the 10′−12′ ring for different closed observations, to check for temporal variations of the NXB. In Fig. A.2 we report the values of broken power-law free parameters (namely the slopes, $\Gamma_1$ and $\Gamma_2$, and the normalization, $N$) for both MOS in the 0.7−10.0 keV band. The scatter of $\Gamma_1$ and $\Gamma_2$ values is the same order of magnitude as the statistical uncertainties, while the scatter of the $N$ values (≈20%) is not purely statistic; i.e., NXB normalization varies for different observations.

We also checked for spatial variations of the internal background. As explained at the beginning of this section, we accumulated the total spectrum for each of the 6 rings and for each instrument. We defined the surface brightness, $SB$, as the ratio between $N$ and the area of the ring. In Fig. A.3 we report MOS1 and MOS2 best fit values of $SB$ as a function of the distance from the center, by fixing $\Gamma_1$ and $\Gamma_2$. The spatial variations are greater than statistical errors but less than 5%. To a first approximation, the NXB is flat over the detector. We find similar results, both in terms of temporal and spatial variations, when fitting spectra above 2 keV.

Emission lines showed rather weak temporal variations and most of them (namely, all except for Al, Si, and Au) have a uniform distribution over the detector. Al lines are more intense in the external CCDs, while Si lines are more intense in the central CCD. Conversely, Au lines are very localized in the outer regions of the field of view, thus we model them only when analyzing rings beyond 3.5′.

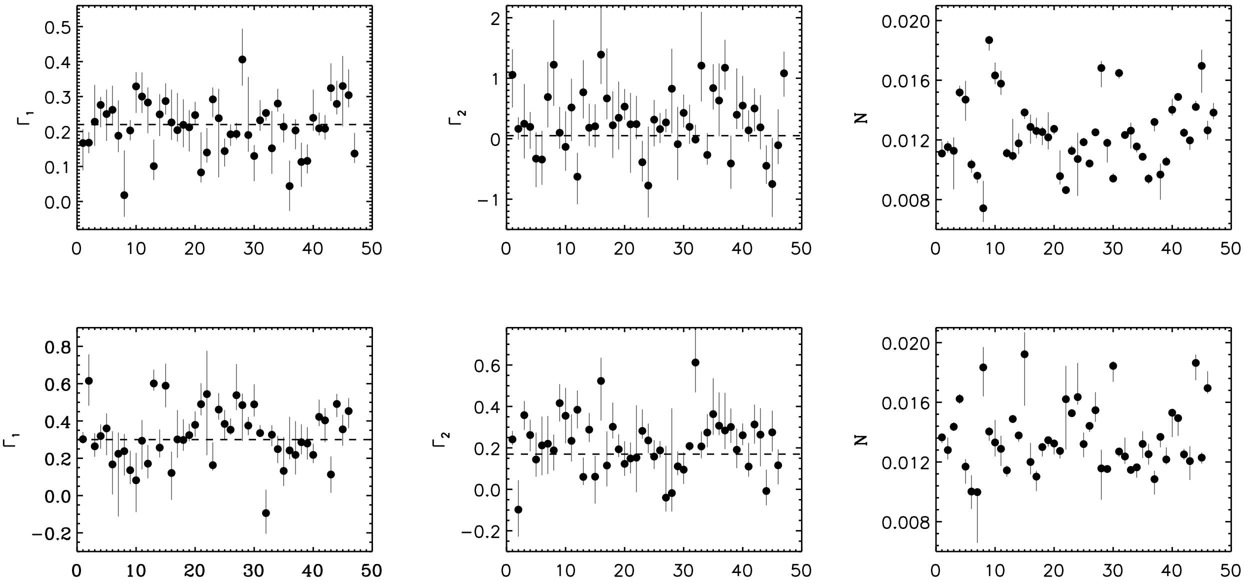

**Fig. A.2.** $\Gamma_1$, $\Gamma_2$, and $N$ values for MOS1 (*top*) and MOS2 (*bottom*) for all closed observations analyzed. The dotted lines are the best fit values reported in Table A.1. For $\Gamma_1$ and $\Gamma_2$ the scatter is comparable with the uncertainties, while for $N$ there is an intrinsic scatter of ≈20%. $N$ values are reported in XSPEC units.

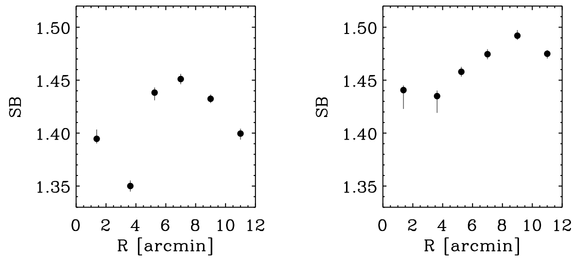

**Fig. A.3.** Surface brightness best fit values for MOS1 (*left*) and MOS2 (*right*) as a function of the distance from the detector center.

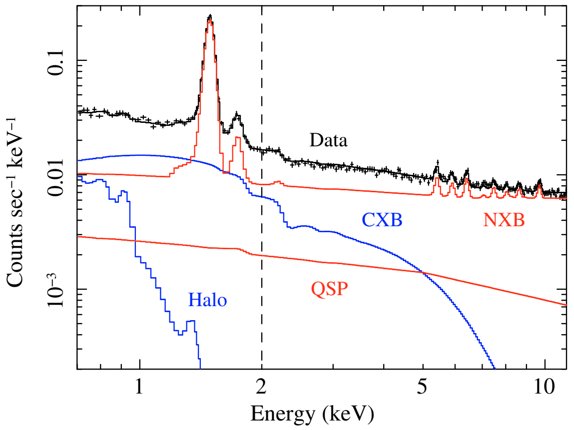

**Fig. B.1.** MOS1 spectrum from blank field observations in the 10′−12′ ring. Above 2 keV the spectrum is simpler.

## Appendix B: The analysis of "blank field" observations

A large number (≈30) of "blank field" observations were analyzed to characterize the spectrum of other background components. Exposure times of individual observations cover between 30 and 90 ks for a total exposure time of ≈600 ks. Almost all observations have different pointing in order to maximize the observed sky region and minimize the cosmic variance of the X-ray background.

Data were prepared and cleaned as described in Sects. 3.1.1 and 3.1.2. For each instrument (i.e. MOS1 and MOS2) and each filter (i.e. THIN1 and MEDIUM), we produced total spectra by summing, channel by channel, spectral counts accumulated during all observations after the selection of the same rings used for closed observations (see Appendix A). We associated the appropriate RMF and ARF to each spectrum and performed a minimal grouping to avoid channels with no counts. We also calculated the average $R_{\rm SB}$ (see Sect. 3.1.2), obtaining $1.09 \pm 0.01$ for both filters and both detectors.

Inside the field of view, the spectral components are the following (see Fig. B.1):

- the X-ray background from Galaxy Halo (HALO);
- the cosmic X-ray background (CXB);
- the quiescent soft protons (QSP);
- the cosmic ray induced continuum (NXB);
- the fluorescence emission lines.

The photon components only (i.e., HALO and CXB) were multiplied by the effective area and absorbed by our Galaxy. The equivalent hydrogen column density along the line of sight, $N_{\rm H}$, was fixed to the 21 cm measurement (Dickey & Lockman 1990), averaged over all fields. We selected blank field observations pointed at high galactic latitude, therefore $N_{\rm H}$ is $<10^{21}$ cm$^{-2}$ and the absorption effect is negligible above 1 keV.

In the 0.7−10.0 keV band, the total model is composed of a thermal component (HALO), a power law (CXB), two broken power laws (QSP and NXB), and several Gaussians (fluorescence emission lines). The thermal model (APEC in XSPEC) parameters are: $kT = 0.197$ keV, $Z = 1.0\ Z_\odot$, and $z = 0.0$ (Kuntz & Snowden 2000). The slope of the CXB power law was fixed to 1.4 (De Luca & Molendi 2004), and the normalization was calculated at 3 keV to minimize the correlation with the slope. The QSP broken power law has a break energy at 5.0 keV, and the slopes were fixed to 0.4 (below 5 keV) and 0.8 (above 5 keV). The model parameters for the internal background are the same as reported in Appendix A. In the 2.0−10.0 keV band the model

**Table B.1.** Best fit results for the analysis of blank field observations in the 10′−12′ ring.

| Instr. | Filter | $N_{\rm HALO}$ $[10^{-4}]$ | $N_{\rm QSP}$ $[10^{-3}]$ | $N^{a}_{\rm CXB}$ $[10^{-2}]$ |
|---|---|---|---|---|
| MOS1 | THIN1 | 1.7 ± 0.1 | 2.4 ± 0.1 | 5.1 ± 0.1 |
| MOS2 | THIN1 | 1.6 ± 0.1 | 2.5 ± 0.1 | 5.0 ± 0.1 |
| MOS1 | MEDIUM | 1.4 ± 0.1 | 2.6 ± 0.1 | 6.0 ± 0.1 |
| MOS2 | MEDIUM | 1.6 ± 0.1 | 2.4 ± 0.1 | 5.8 ± 0.1 |

Notes. [a] calculated at 3 keV.

is simpler (namely, three power laws and several Gaussians) and more stable. The HALO component is negligible above 2 keV, the CXB model is the same as in the 0.7−10.0 keV band, the slope of the QSP power law was fixed to 1.0, and the model parameters for the internal background are those reported in Appendix A.

Most components have rather similar spectral shapes (see Fig. B.1), therefore a high degree of parameter degeneracy is present. In such cases, it is useful to constrain as many parameters as possible. Events outside the field of view are exclusively due to the internal background, therefore the spectrum accumulated in this region provides a good estimate of the NXB normalization, $N_{\rm NXB}$. By analyzing closed (CL) observations we find that the ratio between $N_{\rm NXB}$ calculated in two regions of the detector is independent of the particular observation:

$$\frac{N_{\rm NXB}(R_1;O_1)}{N_{\rm NXB}(R_2;O_1)} = \frac{N_{\rm NXB}(R_1;O_2)}{N_{\rm NXB}(R_2;O_2)}, \tag{B.1}$$

where $R_{1,2}$ are any two regions of the detector, and $O_{1,2}$ are any two observations. By using the region outside the field of view (OUT), for each ring (R) of blank field (BF) observations, we estimated and fixed $N_{\rm NXB}$ from Eq. (B.1):

$$N_{\rm NXB}(R;BF) = N_{\rm NXB}(R;CL) \times \frac{N_{\rm NXB}(OUT;BF)}{N_{\rm NXB}(OUT;CL)}\,. \tag{B.2}$$

In Table B.1 we report the best fit values for the normalization of the HALO, $N_{\rm HALO}$, of the QSP, $N_{\rm QSP}$, and of the CXB, $N_{\rm CXB}$, in the 10′−12′ ring, for MOS1 and MOS2 instruments and for THIN1 and MEDIUM filters. We fit spectra in the 0.7−10.0 keV energy band. We stress the remarkably good agreement between MOS1 and MOS2 for all parameters. Moreover, we point out that, when comparing observations with different filters, values for $N_{\rm HALO}$ and $N_{\rm QSP}$ agree, while values for $N_{\rm CXB}$ are significantly different (≈20%) because of the cosmic variance (≈15% expected for the considered solid angles).

By construction (see Eq. (1)) there is a relation between $R_{\rm SB}$ and $N_{\rm QSP}$, so that the higher $R_{\rm SB}$, the higher $N_{\rm QSP}$. For observations that are not contaminated by QSP, $R_{\rm SB} \approx 1.0$ and $N_{\rm QSP} \approx 0.0$ are expected. Since $R_{\rm SB}$ values span a relatively narrow range (roughly between 1.0 and 1.5), we approximated the relation between $R_{\rm SB}$ and $N_{\rm QSP}$ with a linear function: $N_{\rm QSP} = A \times (R_{\rm SB} - 1)$. The scaling factor, $A \approx 0.03$, was determined from the analysis of blank fields observations, for which we measured $R_{\rm SB} = 1.09 \pm 0.01$ and $N_{\rm QSP} = (2.5 \pm 0.1) \times 10^{-3}$. Thus, for each observation we model the bulk of the QSP component by deriving $N_{\rm QSP}$ from $R_{\rm SB}$ (see Sects. 3.2.1 and 3.2.2). In Sects. 5.1.3 and 5.2.3 we discuss possible systematics related to QSP, and show that the linear approximation used above is satisfactory.

**Table B.2.** Correction factors.

| Ring | HALO | | CXB | |
|---|---|---|---|---|
| | MOS1 | MOS2 | MOS1 | MOS2 |
| 0′−2.75′ | 0.62 | 0.68 | 0.80 | 0.91 |
| 2.75′−4.5′ | 0.74 | 0.70 | 0.70 | 0.78 |
| 4.5′−6′ | 0.63 | 0.65 | 0.89 | 0.95 |
| 6′−8′ | 0.74 | 0.71 | 0.89 | 0.92 |

As mentioned in Sect. 3.2.1, we estimated the normalizations of the background components in the 10′−12′ ring, and rescaled them in the inner rings. When considering the 0.7−10.0 keV energy band, a simple rescaling by the area ratio was too rough and caused systematic errors, especially in the outer regions where cluster emission and background fluctuations are comparable. To overcome this problem, we have proceeded in the following manner. We fit blank field spectra, by fixing $N_{\rm NXB}$ and $N_{\rm QSP}$, and determined $N_{\rm CXB}$ and $N_{\rm HALO}$ best fit values. For each ring and instrument, we defined a correction factor, $K(r)$:

$$K(r) = \frac{N_{\rm obs}}{N_{\rm exp}}, \tag{B.3}$$

where $N_{\rm obs}$ is the best fit value that we just obtained, and $N_{\rm exp}$ was derived by rescaling the value measured in the 10′−12′ ring by the area ratio. In Table B.2 we report the values for $K(r)$ for all cases. $K(r)$ is a second order correction, because the contribution of CXB and HALO components to the total flux is relatively small: when considering the 0.7−2.0 keV band only (i.e. the energy range in which these components are more intense), the HALO-to-total and the CXB-to-total flux ratios are ≈5% and ≈20%, respectively. Thus, the effective correction is of a few percent only, for both cases. Different observations have different centers in detector coordinates, and the intensity of the various components depends on the particular observation. These facts could cause some discrepancies; however, since we analyzed a large number of blank-field and cluster observations, we expect only a few percent systematic effect on the mean profile. When considering the band above 2 keV, the statistical quality of the data is poorer; therefore, rescaling by the area ratio (i.e. no correction factor) can be considered a good approximation for both CXB and NXB. The QSP value wsa rescaled by the soft proton vignetting profile (Kuntz 2006) and did not require any correction factor.

Unfortunately, a precise characterization of the QSP component for EPIC-pn was not possible. Uncertainties on $N_{\rm NXB}$ were very large, because the region outside the EPIC-pn field of view is much smaller than the MOS one, and the presence of a non negligible fraction of out-of-time events introduced a further complication. Moreover, the EPIC-pn background is much less stable than the EPIC-MOS one, especially below 2 keV. The EPIC-pn instrument has further drawbacks due to the electronic board near the detector: the NXB spatial distribution is not flat and the emission due to Ni-Cu-Zn lines (between ≈7.5 keV and ≈9.5 keV) is more intense in the outer rings. For these reasons, as mentioned in Sect. 3, we considered only EPIC-MOS data in our analysis.